Nickel Cobaltite Nanostructures for Photoelectric and Catalytic Applications

*Shaoxiong Liu, Linfeng Hu, Xiaojie Xu, Ahmed A. Al-Ghamdi, and Xiaosheng Fang**

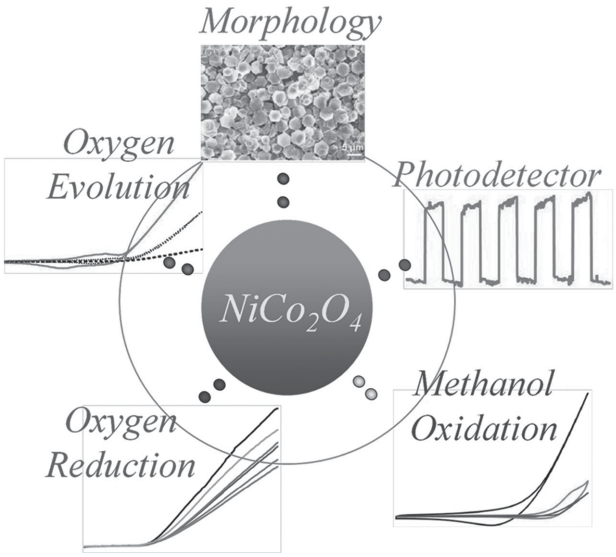

From the Contents

Bimetallic oxide nickel cobaltite ($NiCo_2O_4$) shows extensive potential for innovative photoelectronic and energetic materials owing to their distinctive physical and chemical properties. In this review, representative fabrications and applications of $NiCo_2O_4$ nanostructures are outlined for photoelectronic conversion, catalysis, and energy storage, aiming to promote the development of $NiCo_2O_4$ nanomaterials in these fields through an analysis and comparison of their diverse nanostructures. Firstly, a brief introduction of the spinel structures, properties, and morphologies of $NiCo_2O_4$ nanomaterials are presented. Then, the advanced progress of $NiCo_2O_4$ nanomaterials for both photoelectronic conversion and energy fields is summarized including such examples as solar cells, electrocatalysis, and lithium ion batteries. Finally, further prospects and promising developments of $NiCo_2O_4$ nanomaterials in these significant fields are proposed.

www.MaterialsViews.com

1. Introduction

Cobalt-nickel oxide ($NiCo_2O_4$) is well known as an interesting mixed-valence transition metal oxide semiconductor with a spinel structure. **Figure 1** exhibits the crystallographic structure of $NiCo_2O_4$, in which nickel occupies the octahedral sites and cobalt is distributed over both octahedral and tetrahedral sites.[1–3] The structural formula of $NiCo_2O_4$ has been interpreted comprehensively. King and co-workers proposed the structural formula of $NiCo_2O_4$ in the form of $Co^{2+}_{0.9}Co^{3+}_{0.1}[Co^{3+}_1Ni^{2+}_{0.9}Ni^{3+}_{0.1}]O^{2-}_{3.2}\ O^{-}_{0.8}$.[4] Goodenough's team has investigated ferromagnetic $NiCo_2O_4$ and interpreted the structural formula as $Co^{2+}_{0.35}Co^{3+}_{0.65}\ [Co^{3+}_1Ni^{2+}_{0.65}Ni^{3+}_{0.35}]\ O^{2-}_4$.[3] Lenglet's group has investigated the electronic structure of $NiCo_2O_4$ and proposed the corresponding structural formula in the form of $Co^{2+}_xCo^{3+}_{1-x}\ [Co^{3+}_1Ni^{2+}_{1-x}Ni^{3+}_x]O^{2-}_4$.[2] Both redox couples of the Ni and Co elements, Co^{3+}/Co^{2+} and Ni^{3+}/Ni^{2+}, are present in the main oxidation state of $NiCo_2O_4$ crystals according to the above research. However, there are still other viewpoints which should be taken into account. Iliev and co-workers have investigated the epitaxial thin film of $NiCo_2O_4$ by polarized Raman spectroscopy and found that films grown at temperatures lower than 450 °C can be described by mixed cation/charge distribution at tetragonal and octahedral sites of $NiCo_2O_4$ crystals.[5] Marco and co-workers have reported an unusally high oxidation state of Ni with a valence of +4 in $NiCo_2O_4$, which resulted in a delocalised electron distribution at the octahedral sites with a specific structural formula of $[Ni^{3+}_{0.1}Co^{2+}_{0.9}]_{tet}[Ni^{3.5+}_{0.9}Co^{2.5+}_{1.1}]_{oct}O_4$.[6] Owing to the oxidation states of Ni and Co in $NiCo_2O_4$ still being diverse in different instances, detailed charactizations of $NiCo_2O_4$ should be interpreted cautiously. In the past few years, $NiCo_2O_4$ has been generally believed to be an attractive research topic in the field of materials science with immense potential for a wide variety of fundamental and technological applications.

Sustainable energy production, conversion, and storage have become the primary trend to solve the problem of the energy crisis that the world currently confronts.[7] Numerous highly efficient energy-conversion (such as solar cells, photocatalysis, and electrocatalysis) and storage (such as supercapacitors, lithium-ion batteries, metal–air batteries) systems have been developed to meet this challenge.[8,9] Essentially, the electrode materials play a primary role in the practical performance of those energy systems.[10] Among the various metal oxides widely used in these systems, $NiCo_2O_4$ is of great interest as one of the most promising candidates for electrode materials. For example, compared with pure NiO or Co_3O_4, the $NiCo_2O_4$ has at least 2 orders of magnitude higher electrical conductivity. It has been demonstrated that $Ni_xCo_{3-x}O_4$ and polycrystalline $NiCo_2O_4$ films at 300 °C exhibit an electrical conductivity of 0.1–0.3 S cm^{-1} and 0.6 S cm^{-1}, respectively, while that of hexagonal $NiCo_2O_4$ nanoplates reaches up to 62 S cm^{-1}, which are all much higher than the 3.1×10^{-5} S cm^{-1} of Co_3O_4.[11–15] The high electronic conductivity, which favors fast electron transfer in $NiCo_2O_4$ materials, facilitates their application as electrodes. Meanwhile, simultaneous contributions from both redox couples of Co^{3+}/Co^{2+} and Ni^{3+}/Ni^{2+} offer richer redox reactions than those of the two corresponding single metallic oxides, resulting in a notable catalytic and electrocatalytic activity.[16,17] The electronic structure of $NiCo_2O_4$ is characterized as tetrahedral high spin Co^{2+} ($e_g^4t_{2g}^3$), octahedral low spin Co^{3+} (t_{2g}^6), and Ni^{3+}($t_{2g}^6e_g^1$). Its band structure is composed of O 2p orbitals as a valence band and metal (Ni, Co) 3d orbitals as a conduction band. Superior photocatalytic activity has been found for $NiCo_2O_4$ nanostructures on the basis of their electron configuration and band structure.[18] There are three kinds of electron photoexcitations in $NiCo_2O_4$: 1) from the O 2p orbital to the metal (Ni, Co) 3d-e_g orbital; 2) from the O 2p orbital to the metal (Ni, Co) 3d-t_{2g} orbital; 3) monometal internal electron transtions: from the Co 3d-t_{2g} orbital to the Co 3d-e_g or from the Ni 3d-t_{2g} orbital to the Ni 3d-e_g. The concomitant Co element can cause an electronic effect and impel nickel to a higher oxidation state.[19] This electronic effect will facilitate monometal internal electron transitions and thus improve the photoexication and photocatalyst activity.[20] $NiCo_2O_4$ have been found to exhibit unique magnetic characteristics, with a magnetisation of about 0.8 T, extrapolated to 0 K, consonant with moments from 1.25 to 1.5 μB per formula unit.[21,22] Battle and co-workers have proposed a $NiCo_2O_4$ model based on neutron diffraction experiments, in which the magnetic $NiCo_2O_4$ is composed of magnetic Co^{2+} together with nonmagnetic Co^{3+} at the tetragonal sites and magnetic Ni^{3+} together with nonmagnetic Ni^{2+} at the octahedral sites.[3] Accordingly,

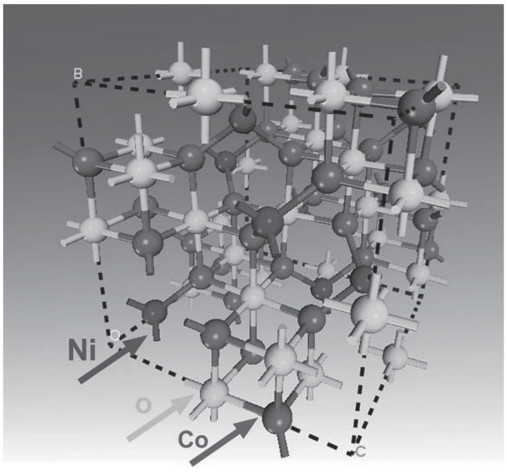

Figure 1. Crystal structure of $NiCo_2O_4$ unit cell with a spinel structure. Reproduced with permission.[1] Copyright 2012, Royal Society of Chemistry.

Dr. S. X. Liu, Prof. L. F. Hu, X. J. Xu, Prof. X. S. Fang
Department of Materials Science
Fudan University
Shanghai 200433, P. R. China
E-mail: xshfang@fudan.edu.cn
Dr. A. A. Al-Ghamdi, Prof. X. S. Fang
Department of Physics
Faculty of Science
King Abdulaziz University
Jeddah 21589, Saudi Arabia

DOI: 10.1002/smll.201500315

small NANO MICRO

the cationic distribution in $NiCo_2O_4$ regulates the magnetic behavior and causes a magnetic phase conversion from a frustrated dipolar system to an enhanced magnetic ordering in off-stoichiometric nickel cobaltite.[23] The magnetic properties and saturation magnetization of $NiCo_2O_4$ can also be tuned by annealing,[24] morphology,[25] and components.[26] Iliev and co-workers have reported that epitaxial $NiCo_2O_4$ films deposited at temperatures lower than 450 °C are ferrimagnetic, and those grown at elevated temperatures are nonmagnetic.[5] The bulk $NiCo_2O_4$, nanorod $NiCo_2O_4$, and 3 wt% NiO/97 wt% $NiCo_2O_4$ nanocomposite have been found to exhibit strong magnetization with a high saturation magnetization (M_s) of 29, ≈26, and 24 emu g^{-1}, respectively.[25–27] On account of these intrinsic properties and other advantages such as their low cost, rich abundance, and environmental friendliness, $NiCo_2O_4$ materials have been extensively used in the fields of photodetection,[28] photocatalysis,[18] supercapacitors,[29] Li-ion batteries[30] and metal–air batteries,[31] fuel cells,[32] magnetic devices,[33] flat-panel displays,[12] ferrofluid technologies,[34] drug delivery,[35] optical limiters and switches,[36] infrared transparent conducting materials,[24] heterogeneous catalysis,[16] and various electrochemical reactions, for example: Cl_2 evolution,[37] O_2 evolution (OER),[38] O_2 reduction reaction (ORR),[39] H_2O_2 reduction,[40] methanol oxidation,[41] and electrochemical sensors.[42]

The extensive applications of $NiCo_2O_4$ has encouraged the exploration of precise syntheses of particular $NiCo_2O_4$ nanostructures. So far, the synthesis of 1D nanowires,[43,44] nanorods,[25,45] nanotubes,[46] 2D nanosheets,[15,16,18,28,38,47] nanoflakes,[31] and 3D hierarchical structures[48] such as urchin-like structures,[49–53] nanoflowers,[17] and arrays composed of nanowires,[11,54–58] nanorods,[59,60] nanoflakes,[32] and nanosheets,[61] have been comprehensively investigated. One-dimensional $NiCo_2O_4$ nanostructured materials provide efficient pathways for the transport of electrons and ions, leading to faster diffusion kinetics and a higher rate capability for energy-storage applications.[44] Two-dimensional $NiCo_2O_4$ nanostructured materials, usually crosslinking with each other, provide relatively high surface areas for storing more ions and active sites.[62,63] Three-dimensional $NiCo_2O_4$ nanostructured materials tend to be constructed from the above two nano-units with other additional advantages, such as higher stability, better porosity, and aggregation resistance.[64,65] Other than spinel $NiCo_2O_4$, Co^{2+} and Ni^{2+}, because of their similar unit cell structures, also can form homogeneous solid solutions in any molar ratio with a NaCl-type crystal structure as $Co_xNi_{1-x}O$. Yang and co-workers reported NaCl-type $Co_xNi_{1-x}O$ ($0 < x < 1$) nanorods serving as a high-performance electrochemical capacitors with the capacitance reaching a maximum at a 1:1 molar ratio of Co/Ni.[66] The properties of $NiCo_2O_4$ nanostructures are dependent on the method of preparation.[67] Marco and co-workers found that the $NiCo_2O_4$ nanostructures with similar nominal compositions prepared by different methods exhibit notably different Ni^{2+} and Co^{2+} ion distributions.[68] Considering the thermal and structural instability of $NiCo_2O_4$ phases at high temperature, the calcination treatment prevalent in high-temperature syntheses should be manipulated deliberately.[23] Verma and co-workers found a formation of NiO nanoparitcles owing to the partial decomposition of $NiCo_2O_4$ above 673 K.[24] Cabo and co-workers also detected NiO impurities at 550 °C.[69] The calcination temperature will influence the hypostatic consititution and structure of nickel cobaltites directly. Accordingly, much effort should be devoted to the precise preparation method for better performance.

So far, there have been various methods developed to prepare $NiCo_2O_4$ nanostructures in terms of exploiting their unique properties and optimizing novel applications. Here in this article, a selection of recent works on $NiCo_2O_4$ nanostructures is reviewed, with a special focus on the morphology features and novel applications. Firstly, a brief introduction of $NiCo_2O_4$ nanostructures with distinctive morphologies is presented, and then the recent progress in exploiting the unique properties and novel applications of $NiCo_2O_4$ nanostructures are discussed. Finally, the possible challenges and potential opportunities of $NiCo_2O_4$-related materials are proposed.

Shaoxiong Liu received his BS in chemistry from the University of Science and Technology of China (USTC). In 2013, he obtained his PhD at the same university. He joined Prof. X. S. Fang's group at the Department of Materials Science, Fudan University in November 2013 as a postdoctoral fellow. His current research interests include the synthesis, characterization, and applications of semiconductor nanocomposites, focusing on Co-based nanomaterials.

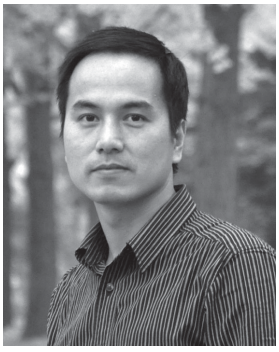

Xiaosheng Fang is currently a professor at the Department of Materials Science at Fudan University, Shanghai, China. He received a PhD from the Institute of Solid State Physics, Chinese Academy of Sciences, in 2006 under the supervision of Prof. Lide Zhang. He has also worked at the National Institute for Materials Science, Japan, and at the International Center for Young Scientists-International Center for Materials Nanoarchitectonics. He currently researches the controlled fabrication, properties, and optoelectronic applications of semiconductor nanostructures, with a focus on inorganic semiconductor nanostructure-based optoelectronic devices.

2. Synthesis of $NiCo_2O_4$ Nanostructures

Due to the superior physical and chemical properties compared to their bulk materials, nanocrystals have attracted growing interest for both their fabrication and application. Therefore, morphologically controllable synthetic methods aiming for well-defined nanocrystals are the primary step. So far, the main synthesis strategies include liquid-phase co-precipitation,[43,70] hydro- and solvothermal routes,[1,41,71] microwave-assisted methods,[72] electrodeposition methods,[32] electrospinning methods,[73] high-temperture

synthesis[23,24,69] etc. In order to comprehensively understand $NiCo_2O_4$ nanostructures, **Table 1** lists an up-to-date summary of the typical synthetic approaches and special properties of $NiCo_2O_4$ nanostructures. With the advantages of easy handling, low temperature, inexpensive equipment, and large-scale production, solution methods such as hydro- and solvothermal routes, microwave-assisted methods, and liquid-phase co-precipitation have become the most widely applicable strategies, as shown in the table.

$NiCo_2O_4$ nanostructures exhibit diverse morphologies, including 0D, 1D, 2D, and 3D hierarchical nanostructures and nanoarrays. The 0D $NiCo_2O_4$ nanostructures include mesoporous microspheres,[30] mesoporous hollow sub-microspheres,[70] and hollow crossed nanocubes.[74] Microspheres (**Figure 2**a) and hollow sub-microspheres (Figure 2b) are fabricated by template-free solvothermal and template-engaged synthetic methods with large specific surface areas of 40.58 and 116 $m^2\ g^{-1}$, respectively. The two kinds of microsphere structures both consist of numerous nanoparticles as subunits, while the surface of hollow sub-microspheres is much rougher with some wrinkles of about 4 nm. These built-up features are mesoporous in textual property with pore volumes of 0.217 and 0.51 $cm^3\ g^{-1}$, respectively. Hollow crossed $NiCo_2O_4$ nanocubes (Figure 2c) have been fabricated by simultaneously coordinating etching, precipitation, and subsequent calcination.[74] The $NiCo_2O_4$ nanocubes are uniformly about 500 nm with a 40 nm-thick shell consisting of nanocrystal subunits of 6 nm. With a surface area of 82.25 $m^2\ g^{-1}$ and a pore volume of 0.242 $cm^3\ g^{-1}$, a loose mesoporous structure is documented, which not only maintains the active nanoscale effect, but also favors buffering of the electrode volume changes during electrochemical reactions for Li-ion batteries.

One-dimensional $NiCo_2O_4$ nanostructures include nanorods (Figure 2d,e),[25,45] nanowires (Figure 2f,g),[43] and nanotubes (Figure 2h),[46] whose lateral dimensions are in the range of several hundred nanometers to several

Table 1. A comprehensive, up-to-date summary of the synthesis of $NiCo_2O_4$ nanostructures. ITO (indium tin oxide), SW/MWCNT (single-walled/multiwalled carbon nanotubes), RGO (reduced graphene oxide).

$NiCo_2O_4$ nanostructure	Synthesis	Precursors	Substrate	Application	Ref.
mesoporous microspheres	hydrothermal method	$NiCl_2$, $CoCl_2$	–	anode material for Li-ion batteries	[30]
hollow sub-microspheres	coprecipitation synthesis	$Ni(NO_3)_2$, $Co(NO_3)_2$	silica spheres	supercapacitors	[70]
hollow crossed nanocubes	coordinating etching and precipitation	$NiCl_2$, $CoCl_2$	Cu_2O templates	anode material for Li-ion batteries	[74]
nanorods	hydrothermal method	$Ni(NO_3)_2$, $Co(NO_3)_2$	–	cathode materials for Li–O_2 batteries	[45]
nanorods	surfactant-mediated reverse micellar route	$Ni(NO_3)_2$, $Co(NO_3)_2$	–	electrocatalytic oxygen evolution	[25]
nanowires	coprecipitation synthesis	$Ni(NO_3)_2$, $Co(NO_3)_2$	Ni foam	supercapacitors	[43]
nanowires	polyethylene glycol-directed technique	$Ni(NO_3)_2$, $Co(NO_3)_2$	–	supercapacitors	[44]
nanotubes	electrospinning technique	$Ni(NO_3)_2$, $Co(NO_3)_2$	–	supercapacitors	[46]
hexagonal nanoplatelets	thermal transformation	Co_2Ni_1-LDH	–	photodetectors	[28]
core-ring structured nanoplatelets	hydroxide decomposition	$Ni(NO_3)_2$, $Co(NO_3)_2$	–	photocatalysis	[18]
mesoporous nanoflakes	–	-	–	cathode materials for Li–O_2 batteries	[31]
mesoporous nanoparticles	hydrothermal method	$Co(NO_3)_2$, $Ni(NO_3)_2$	–	CH_3OH electro-oxidation, H_2O_2 electro-reduction	[41]
porous nanosheets	hydrothermal method	$Ni(NO_3)_2$, $Co(NO_3)_2$	–	CO oxidation	[16]
macroporous sheets	hydrothermal method	$Ni(NO_3)_2$, $Co(NO_3)_2$	–	oxygen reduction reaction	[47]
nanosheets	solvothermal method	$Ni(NO_3)_2$, $Co(NO_3)_2$	carbon fiber paper	supercapacitors	[71]
aerogels	epoxide addition procedure	$Ni(NO_3)_2$, $Co(NO_3)_2$	–	electrocatalytic oxygen evolution	[125]
aerogels	epoxide-addition procedure	$NiCl_2$, $CoCl_2$	–	supercapacitors	[145]
urchin-like nanostructures	hydrothermal method	$CoCl_2$, $NiCl_2$	–	psuedocapacitors, photoelectrochemical cells	[1]
urchin-like nanostructures	hydrothermal method	$Ni(NO_3)_2$, $Co(NO_3)_2$	–	supercapacitors	[52]
sea urchinlike porous materials	hydrothermal method	$NiCl_2$, $CoCl_2$	–	supercapacitors	[53]
flower-like superstructures of porous nanosheets	hydrothermal method	$Ni(NO_3)_2$, $Co(NO_3)_2$	–	oxygen reduction reaction	[17]
urchin-like multiple hierarchical structures, flower-like structures	hydrothermal method	$NiCl_2$, $CoCl_2$	Ni foam	supercapacitors	[75]
nanorod arrays	hydrothermal disposition route	$Ni(NO_3)_2$, $Co(NO_3)_2$	Cu	anode material for Li-ion batteries	[59]
nanowire arrays	hydrothermal method	$Ni(NO_3)_2$, $Co(NO_3)_2$	carbon cloth	cathode materials for Li–O_2 batteries	[54]
nanowire arrays	ammonia-evaporation-induced growth	$Co(NO_3)_2$, $Ni(NO_3)_2$	Ti foil	electrocatalytic oxygen evolution	[11]
nanowire arrays	co-precipitation route	$Ni(NO_3)_2$, $Co(NO_3)_2$	–	oxygen reduction reaction, electrocatalytic oxygen evolution	[56]

Continued

Table 1. Continued.

$NiCo_2O_4$ nanostructure	Synthesis	Precursors	Substrate	Application	Ref.
nanowire arrays	hydrothermal method	$NiCl_2$, $CoCl_2$	Carbon textiles	supercapacitors, anode material for Li-ion batteries	[57]
nanowire arrays	hydrothermal method	$NiCl_2$, $CoCl_2$	Ni foam	supercapacitors	[58]
nanoflake arrays	electrodeposition method	$Co(NO_3)_2$, $Ni(NO_3)_2$	stainless steel, ITO	CH_3OH electro-oxidation	[32]
nanosheets	co-electrodeposition	$Ni(NO_3)_2$, $Co(NO_3)_2$	Ni Foam	supercapacitors	[62]
nanosheet arrays	co-precipitation method	$Ni(NO_3)_2$, $Co(NO_3)_2$	Ni foam, Ti foil, stainless-steel foil, and flexible graphite paper	supercapacitors	[80]
nanosheet arrays	electrodeposition	$Ni(NO_3)_2$, $Co(NO_3)_2$	carbon fabric	supercapacitors	[61]
nanowire and nanosheet arrays	hydrothermal method	$Ni(NO_3)_2$, $Co(NO_3)_2$	carbon cloth	supercapacitors	[81]
nanowire and nanosheet arrays	solvothermal route	$Ni(NO_3)_2$, $Co(NO_3)_2$	carbon fiber paper	supercapacitors	[82]
nanorod and nanoflake arrays	chemical bath deposition	$Ni(NO_3)_2$, $CoCl_2$	ITO	supercapacitors	[83]
nanorod arrays and nanosheets on carbon nanofibers	co-precipitation method	$Ni(NO_3)_2$, $Co(NO_3)_2$	carbon nanofibers	supercapacitors	[60]
nanoflake–nanowire arrays	hydrothermal method	$Ni(NO_3)_2$, $Co(NO_3)_2$	Ni foam	supercapacitors	[63]
nanoleaf@nanoflake arrays	hydrothermal method and chemical bath deposition	$Ni(NO_3)_2$, $Co(NO_3)_2$	Ni foam	supercapacitors	[84]
nanosheet@hollow microrod arrays	electrodeposition	$Ni(NO_3)_2$, $Co(NO_3)_2$	Ti foil	supercapacitors	[146]
nanosheet@ nanorod core–shell arrays	co-electrodeposition	-	Ni foam	supercapacitors	[85]
$NiCo_2O_4$/C nanocomposites	hydrothermal method	$Ni(NO_3)_2$, $Co(NO_3)_2$	-	anode material for Li-ion batteries	[144]
$NiCo_2O_4$/CNT hybrids	hydrothermal method	$Ni(NO_3)_2$, $Co(NO_3)_2$	-	oxygen reduction reaction	[124]
$NiCo_2O_4$–SWCNT nanocomposites	hydrothermal method	$Co(NO_3)_2$, $NiCl_2$	-	supercapacitors	[88]
multiwall carbon nanotube/ $NiCo_2O_4$ core–shell nanostructures	electrochemical deposition	$Ni(NO_3)_2$, $Co(NO_3)_2$	stainless steel foil	supercapacitors	[147]
MWCNT@$NiCo_2O_4$ core–shell hybrids	co-precipitation method	$NiCl_2$, $CoCl_2$	-	supercapacitors	[148]
graphene-based $NiCo_2O_4$ nanosheet arrays	hydrothermal method	$Ni(NO_3)_2$, $Co(NO_3)_2$	Ni foam	anode material for Li-ion batteries	[89]
$NiCo_2O_4$ nanoplate–RGO sheet composites	hydrothermal method	$NiCl_2$, $CoCl_2$	-	anode material for Li-ion batteries	[90]
N-doped porous graphene–$NiCo_2O_4$ hybrid papers	heterogeneous reaction method	$Ni(NO_3)_2$, $Co(NO_3)_2$	-	electrocatalytic oxygen evolution	[106]
$NiCo_2O_4$–reduced graphene oxide nanocomposites	hydrothermal method	$Ni(NO_3)_2$, $Co(NO_3)_2$	-	electrocatalytic oxygen evolution	[127]
mesoporous nanoplatelets and graphene sheet hybrids	concurrent precipitation and hydrothermal reactions	$Ni(NO_3)_2$, $Co(NO_3)_2$	-	oxygen reduction reaction, electrocatalytic oxygen evolution	[105]
$NiCo_2O_4$–graphene nanocomposites	co-precipitation method	–	–	supercapacitors	[149]
$NiCo_2O_4$–RGO nanocomposites	in-situ transformation	$Ni(NO_3)_2$, $Co(NO_3)_2$	–	supercapacitors	[150]
$NiCo_2O_4$–graphene oxide nanocomposites	microwave-assisted synthesis	$Ni(NO_3)_2$, Co(NO3)2	–	supercapacitors	[72]
$NiCo_2O_4$@NiO core–shell nanowire arrays	co-precipitation method	$Ni(NO_3)_2$, $CoCl_2$	carbon cloth	supercapacitors	[151]
$NiCo_2O_4$@MnO_2 core–shell nanowire arrays	–	–	Ni foam	supercapacitors	[152]
Co_3O_4@ $NiCo_2O_4$ nanoflakes arrays	co-electrodeposition	$Ni(NO_3)_2$, $Co(NO_3)_2$	Ni foam	supercapacitors	[153]

micrometers. The synthetic parameters, such as surfactants, reaction and calcination temperatures and templates, play an important role in the product morphology. A hydrothermal route followed by low-temperature calcination has been developed for the direct synthesis of porous $NiCo_2O_4$ nanorods (Figure 2d).[45] Every nanorod is composed of ultrafine nanocrystals in the range of 4.0 to 6.0 nm, exhibiting a polycrystalline characteristic. Through a surfactant-mediated reverse micellar method, the aspect ratio of $NiCo_2O_4$ nanorods (Figure 2e) can be tuned from high (about 12) to low (about 5) by using different surfactants.[25] The surfactant effect originates from the textural structure of $NiCo_2O_4$ nanorods, which consists of aligned nanoparticles. While using CTAB (cetyltrimethylammoniumbromide) as surfactant, the smallest nanoparticles are obtained and compose $NiCo_2O_4$ rods with the highest aspect ratio.

Two-dimensional (2D) nanostructures are nanoscale crystals with a single dimension confined, such as nanosheets,

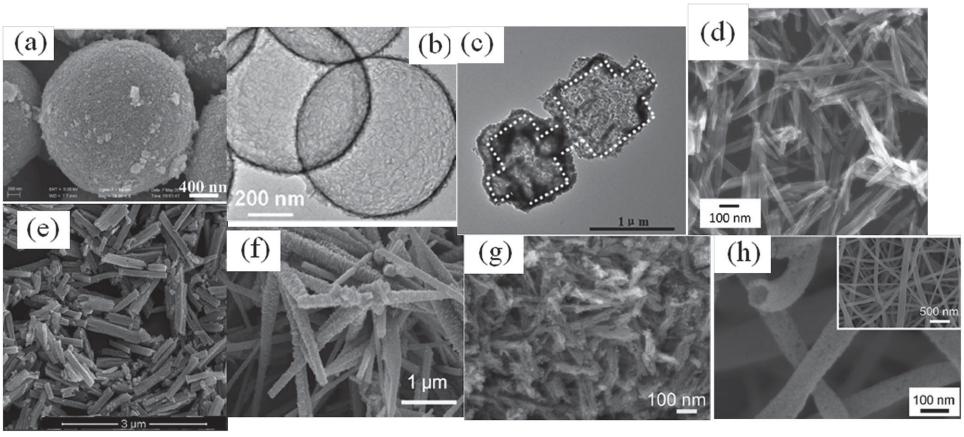

Figure 2. a) TEM (transmission electron microscopy) images of $NiCo_2O_4$ mesoporous microspheres. Reproduced with permission.[30] Copyright 2013, American Chemical Society. b) TEM images of hollow $NiCo_2O_4$ sub-microspheres. Reproduced with permission.[70] Copyright 2013, Royal Society of Chemistry. c) TEM images of hollow crossed $NiCo_2O_4$ nanocubes. Reproduced with permission.[74] Copyright 2014, Royal Society of Chemistry. d) SEM images of $NiCo_2O_4$ nanorods: Reproduced with permission.[45] Copyright 2014, Elsevier Science. e) FESEM (field-emission scanning electronic microscopy) images of $NiCo_2O_4$ nanorods. Reproduced with permission.[25] Copyright 2013, Royal Society of Chemistry. f) FESEM images of ultralayered mesoporous $NiCo_2O_4$ nanowires. Reproduced with permission.[43] Copyright 2012, Royal Society of Chemistry. g) SEM image of porous $NiCo_2O_4$ nanowires. Reproduced with permission.[44] Copyright 2012, Royal Society of Chemistry. h) SEM (scanning electronic microscopy) images of porous $NiCo_2O_4$ nanotubes. Reproduced with permission.[46] Copyright 2013, Wiley-VCH.

nanoflakes, nanowalls, and so on. We have fabricated hexagonal $NiCo_2O_4$ nanoplatelets (**Figure 3**a) by thermal transformation from the corresponding layered double hydroxide (LDH) precursor.[15,28] Every individual $NiCo_2O_4$ nanoplatelet is a single crystal with an average thickness of about 70 nm, and its hexagonal surface corresponds to the (111) plane, indicating that each $NiCo_2O_4$ nanoplatelet is aligned parallel to the substrate surface with a preferred orientation along the [111] direction. Hexagonal core-ring $NiCo_2O_4$ nanoplates (Figure 3b) have also been obtained from a hydroxide decomposition method, with different elemental distributions.[18,38] The ring maintains the stoichiometric $NiCo_2O_4$ spinel structure while the core is enriched with Co, displaying a $Ni_xCo_{3-x}O_4$ spinel phase. Porous $NiCo_2O_4$ nanoflakes and nanosheets have been reported to be synthesized by a hydrothermal method and subsequent thermal decomposition at elevated temperatures.[16,31,41,47] Figure 3c shows macroporous $NiCo_2O_4$ sheets with a thickness of about 150 nm and pore volumes of up to 0.23 $cm^3\ g^{-1}$, which can facilitate mass transport and accommodate more active surface sites.[47]

Three-dimensional (3D) $NiCo_2O_4$ hierarchical structures are usually constructed with 1D or 2D nanostructures as building blocks, in which urchin-like structures of nanowires, nanorods, and flower-like structures creating nanosheets are most conventional. So far, hydrothermal routes are the major means to prepare this kind of $NiCo_2O_4$ superstruc-

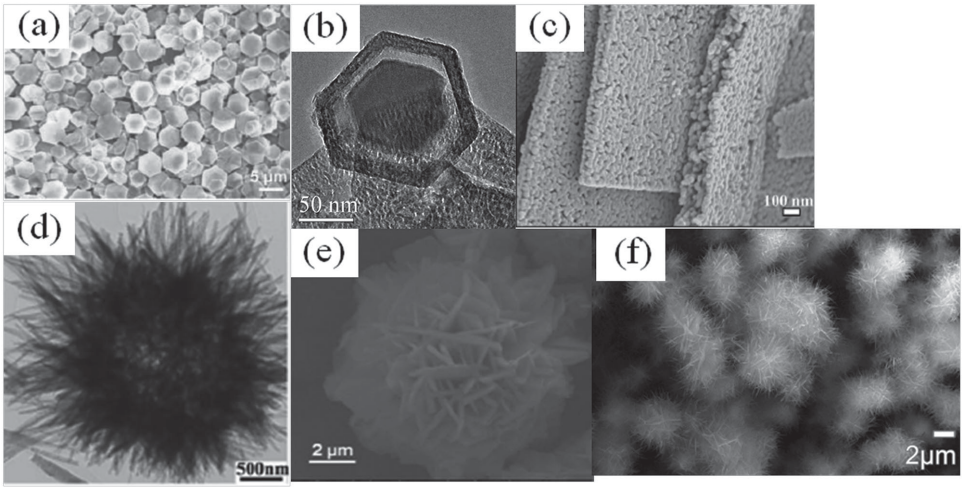

Figure 3. a) SEM images of $NiCo_2O_4$ nanoplatelets. Reproduced with permission.[28] Copyright 2011, Wiley-VCH. b) TEM image of core-ring structured $NiCo_2O_4$ nanoplatelets. Reproduced with permission.[18] Copyright 2009, American Chemical Society. c) FESEM images of macroporous $NiCo_2O_4$ sheets. Reproduced with permission.[47] Copyright 2013, Wiley-VCH. d) FESEM images of urchin-like $NiCo_2O_4$ structures. Reproduced with permission.[53] Copyright 2011, Royal Society of Chemistry. e) SEM images of $NiCo_2O_4$ flower-like structures. Reproduced with permission.[17] Copyright 2013, Royal Society of Chemistry. f) FESEM images of $NiCo_2O_4$ multiple hierarchical structures on Ni foam. Reproduced with permission.[75] Copyright 2014, American Chemical Society.

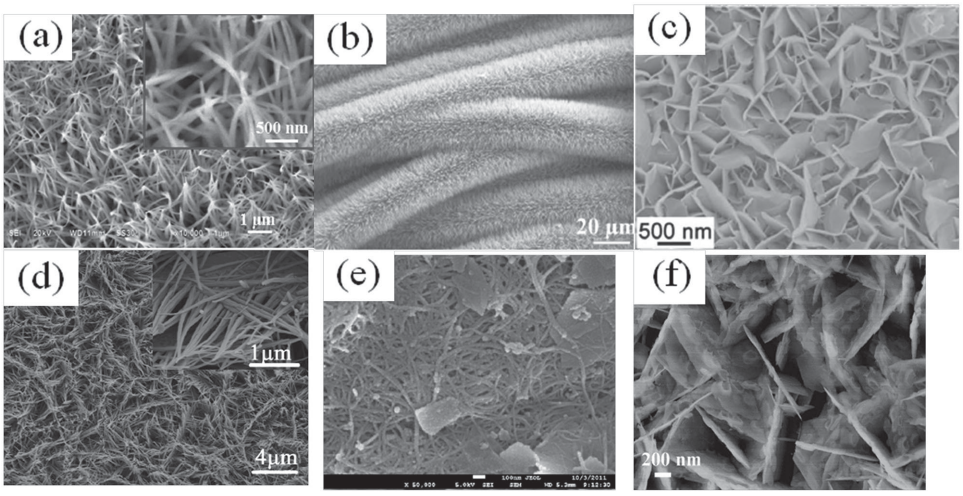

Figure 4. a) SEM images showing the top surface of the $NiCo_2O_4$ nanorod arrays on a Cu substrate. Reproduced with permission.[59] Copyright 2013, Royal Society of Chemistry. b) SEM images of crystalline $NiCo_2O_4$ NWAs (nanowire arrays) /carbon textile composite. Reproduced with permission.[57] Copyright 2014, Wiley-VCH. c) SEM images of $NiCo_2O_4$ nanosheets on Ni foam. Reproduced with permission.[80] Copyright 2013, Wiley-VCH. d) SEM images of nanoflake–nanowire heterostructure arrays on Ni foam. Reproduced with permission.[63] Copyright 2013, Elsevier Science. e) FESEM images of $NiCo_2O_4$–single wall carbon nanotube nanocomposites. Reproduced with permission.[88] Copyright 2012, American Chemical Society. f) SEM image of $NiCo_2O_4$/graphene nanosheets on Ni foam. Reproduced with permission.[89] Copyright 2014, Elsevier Science.

ture.[1,17,52,53,75] By a simple hydrothermal route without templates, Shen and co-workers fabricated $NiCo_2O_4$ urchins with a large surface area of 99.3 $m^2\ g^{-1}$.[1] The urchin-like $NiCo_2O_4$ structures were composed of small nanorods grown around the center following a "nanorod-to-strawbundles-to-urchin spheres" transformation, which is commonly observed in other materials systems during the crystal growth process, such as carbonates, silicates, and tungstates.[76,77] Meanwhile, Yang and co-workers reported the fabrication of urchin-like Ni–Co carbonate hydroxide through a sequential crystallization process and its consequent conversion to porous urchin-like $NiCo_2O_4$ structures (Figure 3d).[53] Comparing this with the method of co-precipitation and thermal decomposition, this strategy offers a superior porous structure with a high specific surface area of up to 198.9 $m^2\ g^{-1}$ and a pore volume of 0.4599 mL g^{-1}. Chen and co-workers prepared hierarchical flower-like $NiCo_2O_4$ structures (Figure 3e) composed of porous nanosheets with morphologies depending on the hydrothermal reaction time.[17] As the reaction time increases from 3 to 12 h, the products change from nanosheets to nanocubes to nanoflowers. Among those nanostructures, the $NiCo_2O_4$ nanoflowers exhibit the largest specific surface area of 88.85 $m^2\ g^{-1}$ and the highest pore volume of 0.28 mL g^{-1}, indicating the important tuning effect of hydrothermal reaction time on the product morphology. By employing a two-step hydrothermal preparation and subsequent annealing procedures, Li and co-workers fabricated 3D $NiCo_2O_4$ multiple hierarchical structures (Figure 3f), urchin-like structures, and flower-like structrues.[75] The multiple hierarchical structures are composed of 1D nanowires and 2D nanosheets, with nanosheets serving as backbones and nanowires enclose them. During the hydrothermal process, the nanowires grow directly on the Ni foam and interconnect in the first step, and the nanosheets are formed among the interspaces between the nanowires and impel the growth of multiple hierarchical structures in the second step. The reverse of the two-step only obtains urchin-like or flower-like structures with a much lower surface area of 42.4 $m^2\ g^{-1}$ compared to that of multiple hierarchical structures (118.3 $m^2\ g^{-1}$), indicating the irreversibility of the growth process. This two-step hydrothermal preparation method not only can be used to obtain a favourable mesoporous structures, but also provides a convenient route to fabricate multiple hierarchical structures.

Recently, hierarchical $NiCo_2O_4$ nanoarrays directly grown on a current collector have been considered a promising solution in energy conversion and storage devices with the distinct advantages of buffering the volume change, fast charge/discharge, and a large contact area with the electrolyte.[78,79] The hierarchical $NiCo_2O_4$ nanoarrays include nanorods,[59] nanowires,[58] nanoflakes,[32] and nanosheets fabricated on varieties of substrates, such as Cu foil, Ni foam, Ti foil, ITO (indium tin oxide), stainless-steel foil, carbon cloth, carbon fiber paper, and so on. For example, Li and co-workers reported the fabrication of $NiCo_2O_4$ nanorod arrays on Cu substrates (**Figure 4**a) by a hydrothermal desposition route.[59] The nanorods were about 100–200 nm in diameter and several micrometers in length, well aligned to a dense array on a Cu substate surface. The $NiCo_2O_4$ nanoarray can be grown not only on even substrates, but also on a cylindrical substrate. Zhang and co-workers fabricated mesoporous $NiCo_2O_4$ nanowire arrays on carbon textiles (Figure 4b) with good flexibility.[57] Lou and co-workers developed a feasible solution method to fabricate $NiCo_2O_4$ nanosheet arrays on Ni foam (Figure 4c) with a large surface area of up to 112.6 $m^2\ g^{-1}$.[80] This facile route can be applied to other conductive substrates, such as Ti foil, stainless-steel foil, and flexible graphite paper, indicating its outstanding versatility. Meanwhile, Lou's group also prepared $NiCo_2O_4$ nanorod and nanosheet arrays/carbon nanofiber hybrid nanostructures by easily altering the additives in the solution methods.[60] Similar universal routes for fabricating $NiCo_2O_4$ nanowire and nanosheet arrays on conductive substrates have also been reported by Wang's, Yu's and Ahn's groups.[81–83] Homogeneous

$NiCo_2O_4$ composites have further increased the diversity of $NiCo_2O_4$ nanoarrays. By a one-step hydrothermal method, Tu and co-workers synthesized nanoflake–nanowire heterostructure arrays (Figure 4d) on Ni foam, with nanowries standing on the edges of the nanosheets.[63] By a two-step strategy with nanosheet arrays first prepared and subsequently serving as secondary substrates for other active mateials, $NiCo_2O_4$ leaf-like nanoflake@nanosheet arrays[84] and nanorod@nanosheet arrays[85] can be fabricated with high maneuverability, which may be used for other complex heterostructure arrays.

In order to tune the intrinsic properties and enhance device performance, a key strategy is to develop composite structures of $NiCo_2O_4$ and other organic or inorganic materials. Carbon nanotubes and graphene, with the advantages of good electron transport, large surface area, high mechanical strength and flexibility, and strong thermal/chemical stability,[86,87] are the materials of choice to serve as ideal substrates for supporting $NiCo_2O_4$ nanostructures. Lee and co-workers fabricated $NiCo_2O_4$–single wall carbon nanotube (SWCNT) structures (Figure 4e) through a hydrolysis process in an ethanol–water system.[88] In order to avoid agglomeration, the ratio of ethanol to water was controlled to obtain a uniform coating of $NiCo_2O_4$ on SWCNTs. Xu and co-workers fabricated graphene-based $NiCo_2O_4$ nanosheet arrays on Ni foam (Figure 4f), with the nanosheets aligned vertically and graphene incorporated among the interspaces.[89] Wang and co-workers decorated hexagonal $NiCo_2O_4$ nanoplates with reduced graphene oxide (RGO) with oriented growth.[90] The Co^{2+} and Ni^{2+} ions were anchored on the graphene nanosheets by oxygen-containing groups to form coprecipitate nanocrystals, which act as nuclei for oriented aggregation to hexagonal nanoplates.

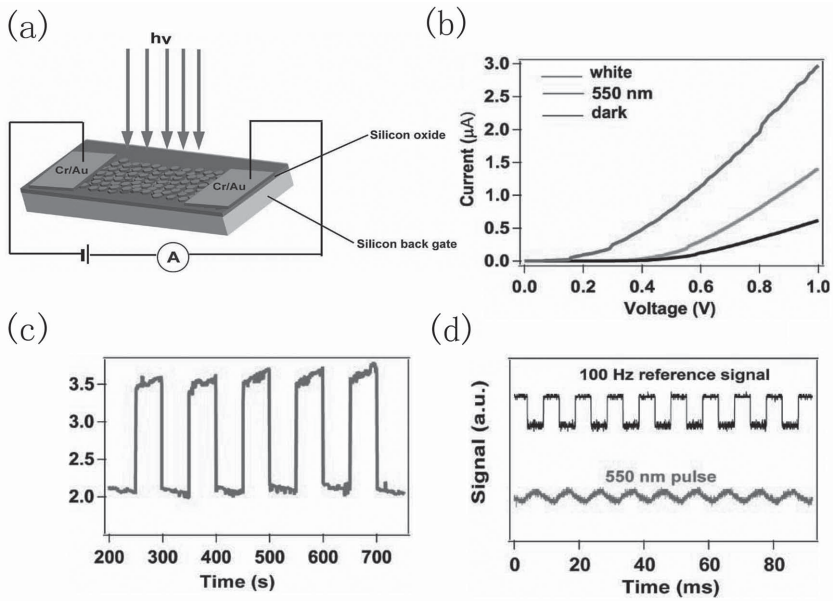

Figure 5. a) Schematics of $NiCo_2O_4$ nanofilm photodetectors, b) *I–V* characteristics of $NiCo_2O_4$ nanofilm photodetectors illuminated with a green light (550 nm, 26.5 μW cm^{-2}) or a white light (343 mW cm^{-2}), c) reproducible on/off switching upon 550 nm light illumination, d) a transient response by illuminating a $NiCo_2O_4$ film with a 550 nm light pulse chopped at a frequency of 100 Hz. Reproduced with permission.[28] Copyright 2011, Wiley-VCH.

3. Novel Properties and Applications of $NiCo_2O_4$ Nanostructures

3.1. Photoelectronic Performance

Recently, as an important binary semiconductor, $NiCo_2O_4$ nanostructures have become immensely attractive due to their unique properties, such as a direct bandgap of about 2.1 eV and excellent photoelectrical properties.[18] The high surface-to-volume ratios and rationally designed morphologies of $NiCo_2O_4$ nanostructures make them promising materials for application in the fields of photoelectric response, such as photodetectors,[28] photoelectrochemical cells,[1] photovoltaic devices,[91] and photocatalysis.[18]

Photodetectors, for photon detection in the visible or ultraviolet regions, has exhibited extensive applications in the field of environmental and biological research, sensors, etc.[92] Semiconductor nanostructures have been used as building blocks for a large number of photodetectors in last few years.[93] Owing to their photoconductive characteristics, semiconductor nanostructures exhibit photosensitivity to light with an energy higher than the bandgap and finally achieve photodetection.[94] As a typical semicomductor oxide, $NiCo_2O_4$ nanostructures have been exploited as promising photodetectors. For example, we fabricated a high-performance $NiCo_2O_4$ nanofilm photodetector with hexagonal $NiCo_2O_4$ nanoplatelets by a simple oil/water interfacial assembly strategy.[28]

The $NiCo_2O_4$ photodetector nanodevice is based on a two-layer $NiCo_2O_4$ nanofilm, which is fabricated from hexagonal $NiCo_2O_4$ nanoplatelets by repeating the oil/water interfacial assembly strategy twice.[95] The high crystal quality of hexagonal $NiCo_2O_4$ nanoplatelets facilitates highly efficient optical absorption and more photogenerated carriers, decreasing the resistance of an individual $NiCo_2O_4$ nanoplatelet.[96] A 2D network of uniform $NiCo_2O_4$ nanoplatelets with a large surface-to-volume ratio also accelerates the combination of photogenerated carriers when the light is switch off, and decreases the decay time.[94] Figure 3a presents a typical image of a two-layer $NiCo_2O_4$ nanofilm, indicating that each $NiCo_2O_4$ nanoplatelet is aligned parallel to the substrate surface with a preferred orientation along the [111] direction to form a compact and continuous nanofilm. The $NiCo_2O_4$ photodetector can be constructed by an electron-beam deposition method as shown in **Figure 5**a, i.e., a two-layer $NiCo_2O_4$ nanofilm is placed on a SiO_2/Si wafer, and two Cr/Au (10 nm/100 nm) electrodes are deposited onto the film by vacuum coating. Figure 5b illustrates the current–voltage (*I–V*) characteristics of the $NiCo_2O_4$ nanofilm photodetector

with and without light illumination. The correlation between current and voltage exhibits nonlinear characteristics, which is interpretted by the Schottky barrier at the metal–semiconductor contacts.[97] As the $NiCo_2O_4$ nanofilm photodetector is illuminated by an incident light with higher energy (above the threshold excitation energy of $NiCo_2O_4$, $E_g \approx 2.10$ eV, 589 nm), the photocurrent displays an obvious enhancement. When the nanofilm photodetector is illuminated by light of 550 nm and white light at the fixed voltage of 1.0 V, the photocurrents are 1.4 μA and 3.0 μA, respectively, which are about 2.3 and 5.0 times larger than the dark current (0.6 μA), indicating the high conversion rate of this nanofilm photedetector. This enhancement is explained by electron–hole pairs excited by the incident light with higher energy than its bandgap and by the desorption of oxygen at the hexagonal $NiCo_2O_4$ nanoplate surface.[98] The photocurrent of $NiCo_2O_4$ nanofilm photodetector (3.0 μA) at a low voltage of 1.0 V under white light is much higher than that of single nanostructure-based photoresponse devices (in the range of a few pA and nA), showing distinct advantages. The origin of this high-performance is that many more nanoplates are involved in the photocurrent collection than for single nanoplate-based devices. Figure 5c presents the time-dependent photoresponse measurement of the $NiCo_2O_4$ nanofilm photodetector by repeatedly turning on and off an incident light of 550 nm at a fixed voltage of 1.0 V. Furthermore, the photocurrent exhibits an excellent stability and a reproduceable feature during plenty of cycles. Both rise and decay times corresponding to light-off-to-light-on and light-on-to-light-off processes are faster than the measurement detection limit (0.3 s). The specific response time characterized by an oscilloscope at 100 Hz (Figure 5d), demonstrates that the rise and decay times of photocurrents are on the scale of milliseconds. The fast response times exhibited by the $NiCo_2O_4$ nanofilm photodetector are significantly shorter than that of all the other semiconductor oxide photodetector devices, which implies its potential application in high-frequency and high-speed photoresponse devices. The variation of the height of the junction barriers while the light is turned on or off has been proposed to be the conceivable mechanism of the fast photoresponse of the $NiCo_2O_4$ nanofilm photodetector. When the light is turned on, the increased carrier density in $NiCo_2O_4$ nanoplates would narrow the barrier width, which is equivalent to a decrease in barrier height.[99] When the light is turned off, the barrier height returns to the original value immediately. The light-induced modulation of the barrier height or barrier width between two adjoining $NiCo_2O_4$ nanoplatelets is a rapid process upon switching the light, resulting in the fast response time for the $NiCo_2O_4$ nanofilm photodetector.

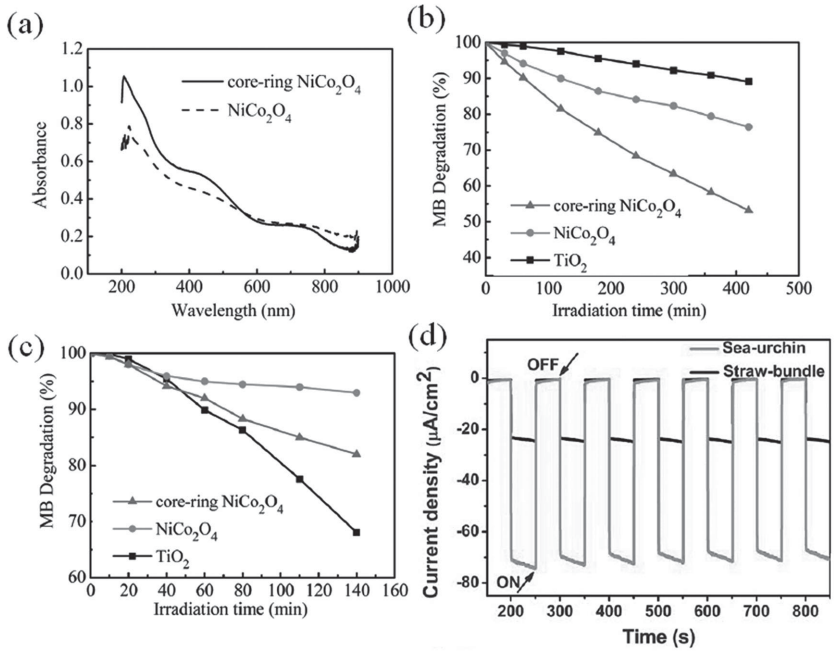

Figure 6. a) UV–vis absorption spectra for the core-ring $NiCo_2O_4$ and $NiCo_2O_4$ (ordinary), b) photocatalytic MB degradation under visible light ($\lambda > 420$ nm) at room temperature over the core-ring $NiCo_2O_4$, $NiCo_2O_4$ (ordinary) and TiO_2 (P25), c) photocatalytic MB degradation under UV light (320 nm < λ < 400 nm) at room temperature over the core-ring $NiCo_2O_4$, $NiCo_2O_4$ (ordinary), and TiO_2 (P25). Reproduced with permission.[18] Copyright 2009, American Chemical Society. d) Photoresponse of urchin-like and straw-like $NiCo_2O_4$ photoelectrodes in PEC tests under one sun illumination rectangle intervals at 0 V bias. Reproduced with permission.[1] Copyright 2012, Royal Society of Chemistry.

Based on this work, the same authors investigated the electrical conduction mechanism of an individual $NiCo_2O_4$ nanoplate.[15] Exponential behavior of temperature-dependent direct current conductivity was found, indicating the semiconducting nature of the $NiCo_2O_4$ hexagonal nanoplate. The electrical conduction mechanism of single $NiCo_2O_4$ nanoplates is found to be dependent on the temperature and explained completely. In the low-temperature rane (T < 100 K), the electrical conduction mechanism is interpreted by Mott's variable-range hopping model. As the temperature increases (T > 100 K), the electrical transport properties are explained in terms of the interactions of variable-range hopping and nearest-neighbor hopping.[100]

Photocatalysis, photoelectrochemical cells, and organic photovoltaics utilizing solar energy, either to activate chemical reactions or for energy harvesting, are promising to solve energy and environmentally related issues and have attracted increasing interest recently.[101] With a proper bandgap for visible light absorption and abundant catalytic sites, $NiCo_2O_4$ nanostructures have widespread application. Lin and co-workers have prepared core-ring structured $NiCo_2O_4$ nanoplatelets and systematically investigated their optical properties and photocatalytic activities towards methylene blue (MB) decomposition.[18] The core-ring $NiCo_2O_4$ nanoplatelets (Figure 3b) exhibit better light adsorbance than ordinary $NiCo_2O_4$ powders in the range of 300 to 560 nm (**Figure 6**a). From the UV–vis absorption spectra, the absorption bandgaps of the core-ring $NiCo_2O_4$ nanoplatelets have been calculated to be 2.06 and 3.63 eV, which corresponds to visible and ultraviolet absorptions,

respectivlely. The photodegradation performance of core-ring structured $NiCo_2O_4$ photocatalysts towards the degradation of methylene blue (MB) displays different behavior depending on the incident light (Figure 6b,c). Under UV light, the photocatalytic performance of core-ring $NiCo_2O_4$ photocatalyst is not so outstanding but, under the visible light, the core-ring $NiCo_2O_4$ photocatalyst exhibits a much higher photocatalytic activity than TiO_2 (P25) or ordinary $NiCo_2O_4$ powder. The higher MB degradation efficiency of core-ring $NiCo_2O_4$ hexagonal platelets has been ascribed to the smaller particle size, better photoabsorption, and more active internal electron transitions. This kind of core-ring structured $NiCo_2O_4$ nanoplate can be used as a promising photocatalyst for dye decompositon under visible light. Shen, Chen, and co-workers have fabricated photoelectrochemical cells based on urchin-like and straw-like $NiCo_2O_4$ nanostructures to investigate the photocurrent response and longtime stability.[1] The urchin-like and straw-like $NiCo_2O_4$ nanostructures were coated on fluorine-doped tin oxide (FTO) conducting glasses to create photoelectrodes under solar simulation. Both photoelectrodes of urchin-like and straw-like $NiCo_2O_4$ nanostructures exhibit fast photocurrent responses and excellent stability as the excitation light was turned on and off (Figure 6d). Both kinds of photoelectrodes exhibit excellent long-term stability and steady repeatability. The photoelectrode of urchin-like $NiCo_2O_4$ nanostructures displays a higher photocurrent density of about 70 μA cm^{-2} compared to that of straw-like $NiCo_2O_4$ nanostructures, which is about 20 μA cm^{-2}. The better photoresponse performance of urchin-like $NiCo_2O_4$ nanostructures is ascribed to the smaller charge-transfer impedance, which leads to a faster hole transfer at the electrode/electrolyte interface than that of straw-like $NiCo_2O_4$ nanostructures. Ndione, Ratcliff, Berry, and co-workers comprehensively investigated $Ni_xCo_{3-x}O_4$ thin films as hole-transport interlayers (HTLs) in organic photovoltaic (OPV) devices.[91] The power-conversion efficiency (η) was found to be independent of their conductivities, but correlated to the relative surface hydroxyl concentration of the $Ni_xCo_{3-x}O_4$ HTL. By employing oxygen-plasma treatment and phosphonic acid surface modification on the $Ni_xCo_{3-x}O_4$ HTL, the power-conversion efficiency was improved from 2.46% to 3.4%, which was equivalent to PEDOT:PSS control devices with an η value of 3.3%.[91] These findings demonstrate great potential for the use of $Ni_xCo_{3-x}O_4$ as a promising HTL material for OPV device applications.

3.2. Heterogeneous Catalysis and Electrochemical Catalysis

Spinel-type binary nickel cobaltites ($NiCo_2O_4$) have found extensive application in heterogeneous catalysis and electrocatalysis owing to their intrinsic redox chemistry and tunable physicochemical, morphological properties.[16,102–106] Compared with individual nickel oxide and cobalt oxide, the $NiCo_2O_4$ possesses richer redox porperties (both Ni^{2+} and Co^{3+} are active species) and much higher electronic conductivity.[11] Moreover, the synergistic effect between the Ni and Co components also results in a significant enhancement in catalytic activity compared to that of individual NiO or Co_3O_4.[16] In this section, typical applications of various $NiCo_2O_4$ nanomaterials in heterogeneous catalysis and electrochemical catalysis will be reviewed, emphasizing not only the superior performance but also the comparison between $NiCo_2O_4$ materials and commercial Pt/C catalysts for practical applications.

3.2.1. Heterogeneous Catalysis

CO oxidation at low temperatures is regarded as a typical model of catalysis in critical calculations[107] and it becomes more important in the field of environmental cleaning and lowering automotive emissions.[108] Given the expense and restricted reserves of noble metal catalysts, the development of base metal catalysts with a lower cost and high activity is extremely necessary. Liang and co-workers found that Ni–Co binary oxides exhibit better catalytic performance for CO oxidation than single NiO and Co_3O_4.[16] Depending on the Co content in the whole system, the Ni–Co binary oxides are classed into three kinds of crystal structure types. With Co content percentage less than 20%, NiO type samples exhibit identical cubic crystal structures to pure NiO, with a larger surface area, higher pore volume, and better catalytic activity than the others. Within the Co content range 40–60%, $NiCo_2O_4$ displays a steady lamellar structure. As Co content increases to more than 80%, the sample tends toward Co_3O_4-type with a Co_3O_4-based crystal structure. The synergy effect of Ni–Co binary oxide results in the improvement of the catalyst activity for CO oxidation. The Ni content has a stronger electrostatic interaction with CO molecules and facilitates the penetration and adsorption of CO molecules onto the pore network.[109] The active species Co^{3+}, which oxidizes CO to CO_2, is efficiently activated by Ni^{2+}. Similarly, N_2O decomposition is much enhanced by nickel cobaltite ($Ni_xCo_{1-x}Co_2O_4$) as compared to pure NiO and Co_3O_4 catalysts with the catalyst activity depending on the ratio of Ni^{2+} to Co^{2+}.[104] The improvement of Ni–Co bimetallic oxides is related to the role of Ni content in enhancing the reduction reaction of Co^{3+} to Co^{2+}, decreasing crystallite sizes, and increasing BET values. Buvaneswari and co-workers found that $NiCo_2O_4$ powder efficiently catalyses the reduction of p-nitrophenol to p-aminophenol by $NaBH_4$ at room temperature without any solvent.[102] The feature of yellow p-nitrophenol disappeared within 60 s with the assistance of $NiCo_2O_4$ powder, which is much faster than that of self-decomposition (several hours). It is proposed that the liberation of hydrogen in the hydrolysis reaction of $NaBH_4$ and water is accelerated by $NiCo_2O_4$ powders which, in succession, reduce p-nitrophenol to p-aminophenol actively. The hydride transfer reaction of 4-chloro-1-nitrobenzene to 4-chloro-1-aminobenzene with 2-propanol and NaOH can also be actively catalysed by $NiCo_2O_4$.[103] Conversion to the desired product is very ideal, with 100% selectivity.

3.2.2. Electrochemical Catalysis: Methanol Oxidation Reaction

Direct methanol fuel cells (DMFCs) have been considered a promising candidates as future power sources for portable applications, due to the high energy density, low operating temperature, fertile raw materials, and environmentally friendly nature.[110,111] But the costly anode electrocatalyst for methanol oxidation and its relatively low catalytic activity are

main problems hindering their wide application.[112] Therefore, the exploration of inexpensive and efficient non-noble electrocatalytic materials such as $NiCo_2O_4$ has attracted considerable interest.[113–116]

Xiao and co-workers investigated $NiCo_2O_4$ nanostructures grown on stainless steel (SS) as electrocatalysts for methanol oxidation, exhibiting higher electrocatalytic activity, lower oxidation overpotential, and greater long-term stability than simple NiO and Co_3O_4.[32] The $NiCo_2O_4$ on stainless steel had a high specific surface area (119 $m^2\ g^{-1}$), small pore diameter (5.8 nm), and large pore volume (0.17 $cm^3\ g^{-1}$). The large specific surface area and mesoporous structure of $NiCo_2O_4$/SS not only increased the electrode–electrolyte contact area but also provided sufficient active sites for electrochemical reactions, leading to a faster methanol oxidation reaction. The CV curves of $NiCo_2O_4$/SS, Co_3O_4/SS, and NiO/SS electrodes in 1 M KOH (**Figure 7**a) show typical electrochemical features of redox couples of Co_3O_4/CoOOH and NiO/NiOOH, respectively.[117,118] The broader redox peaks of $NiCo_2O_4$/SS are ascribed to the mixed valence of $NiCo_2O_4$ with two solid-state redox couples, Co^{2+}/Co^{3+} and Ni^{2+}/Ni^{3+}, providing two kinds of active centre for redox reactions.

The redox reaction mechanisms of $NiCo_2O_4$ are illustrated through the following equations (charges balanced):[88,119]

$$NiCo_2O_4 + OH^- + H_2O \rightarrow NiOOH + 2CoOOH + e^- \quad (1)$$

$$CoOOH + OH^- \rightarrow CoO_2 + H_2O + e^- \quad (2)$$

During methanol oxidation Figure 7b, the $NiCo_2O_4$/SS electrode exhibits a high anodic current up to about 50 A g^{-1}, which is a great increase over that of 10 A g^{-1} of the supporting electrolyte. Compared with the Co_3O_4/SS and NiO/SS electrodes, the $NiCo_2O_4$/SS electrode exhibits a lower overpotential and much higher electrocatalytic activity. The reaction mechanism of methanol oxidation on the $NiCo_2O_4$/SS electrode is illustrated in the following equations (charges balanced):[40,120,121]

$$NiCo_2O_4 + OH^- + H_2O \rightarrow NiOOH + 2CoOOH + e^- \quad (3)$$

$$NiOOH + CH_3OH + 1.25O_2 \rightarrow Ni(OH)_2 + CO_2 + 1.5H_2O \quad (4)$$

$$2CoOOH + 2CH_3OH + 2.5O_2 \rightarrow 2Co(OH)_2 + 2CO_2 + 3H_2O \quad (5)$$

The $NiCo_2O_4$/SS electrode exhibits a much smaller decay at the early stage and a more than four-times-higher current density than the Co_3O_4/SS or the NiO/SS electrodes (Figure 7c), implying an excellent long-term stability of the $NiCo_2O_4$/SS electrode. The EIS (electrochemical impedance spectroscopy) plots (Figure 7d) indicate that the $NiCo_2O_4$/SS electrode possesses a faster charge transfer rate and higher tolerance to reaction intermediate poisoning than other electrodes, which may explain the higher catalytic activity of this electrode. Nevertheless, the onset of oxidation potential of $NiCo_2O_4$/SS is still much higher than the commercial Pt/C electrocatalysts, indicating that there is still room for improvement for this non-noble metal oxide.[113] But it is really exciting to notice that the $NiCo_2O_4$ also displays an obvious superiority over Pt/C catalysts. Wang, Ding, and co-workers prepared mesoporous $NiCo_2O_4$ nanoparticles through a sodium dodecyl sulfate (SDS)-assisted soft-template method, which also displayed higher electrochemical stability and superior antipoison characteristics than Pt/C electrocatalysts.[113] In the long-term stability test with chronoamperometry, the $NiCo_2O_4$ electrode with SDS displays a relatively better electrochemical stability (72.3% current retention after 600 s) than the Pt/C catalyst (52.8%). The current decay (from 137 to 115 mA cm^{-2}) of the $NiCo_2O_4$ electrode in the first 20 s is obviously smaller than that of the Pt/C catalyst (from 246 to 138 mA cm^{-2}). The apparent defects and distinct merits of this kind of $NiCo_2O_4$ electrocatalyst for methanol oxidation imply a great potential in both research and applications.

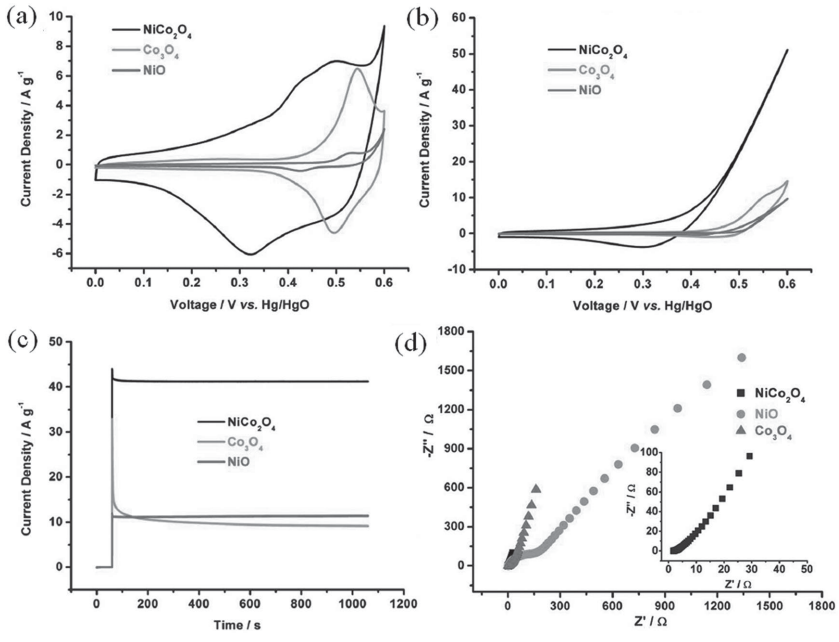

Figure 7. a) CV curves of $NiCo_2O_4$/SS, Co_3O_4/SS, and NiO/SS electrodes in 1 M KOH at a scan rate of 10 mV s^{-1}, b) CV curves of $NiCo_2O_4$/SS, Co_3O_4/SS, and NiO/SS electrodes in 1 M KOH with 0.5 M methanol at a scan rate of 10 mV s^{-1}, c) chronoamperometry curves of $NiCo_2O_4$/SS, Co_3O_4/SS, and NiO/SS electrodes in 1 M KOH, with 0.5 M methanol at 0 V (0–60 s) and 0.6 V (60–1060 s), d) EIS plots of $NiCo_2O_4$/SS, Co_3O_4/SS, and NiO/SS electrodes in 1 M KOH with 0.5 M methanol. Reproduced with permission.[32] Copyright 2013, Royal Society of Chemistry.

3.2.3. Electrochemical Catalysis: Oxygen Reduction and Oxygen Oxidation Reactions

The oxygen evolution reaction (OER) and oxygen reduction reaction (ORR) have played important roles in electrochemical science and technology owing to their wide application in energy storage and conver-

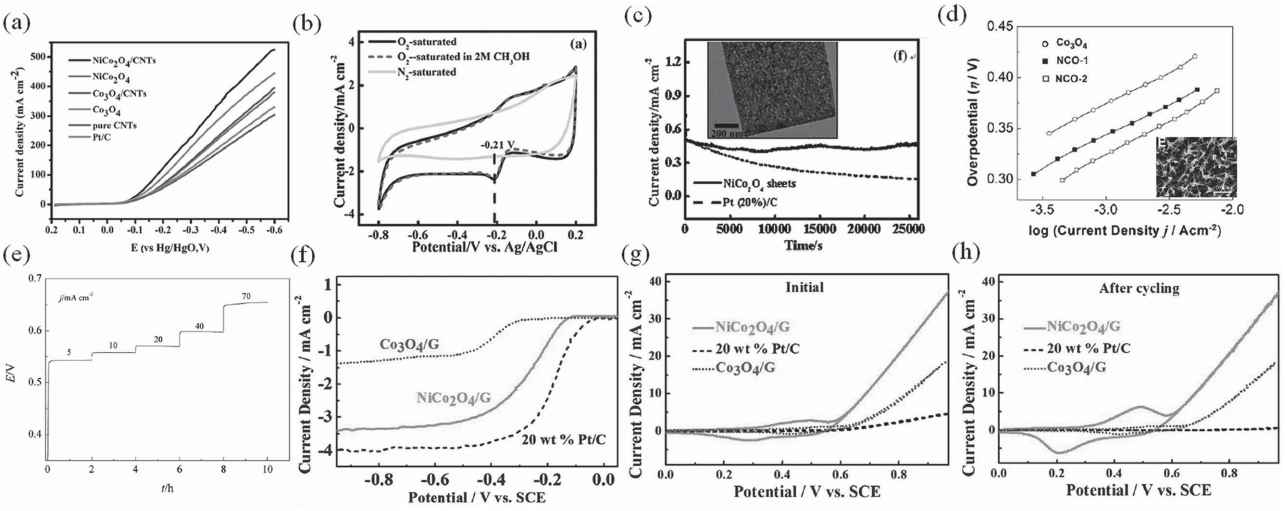

Figure 8. a) Linear polarization curves of air electrodes with different catalysts in 6 M KOH solution at 25 °C. Reproduced with permission.[124] Copyright 2014, Royal Society of Chemistry. b) Cyclic voltammetry curves for 3D macroporous $NiCo_2O_4$ sheet modified electrodes in O_2-saturated, N_2-saturated, 0.1 M KOH and O_2-saturated 2 M CH_3OH with a scan rate of 50 mV s^{-1}. c) Chronoamperometry curves of macroporous $NiCo_2O_4$ sheets and Pt (20%)/C catalysts obtained at −0.3 V in O_2-saturated 0.1 M KOH. Reproduced with permission.[47] Copyright 2013, Wiley-VCH. d) Polarization curves of pure Co_3O_4 NWs, $Ni_xCo_{3-x}O_4$ at 0.5:1 (denoted 'NCO-1'), and $Ni_xCo_{3-x}O_4$ at 1:1 (denoted 'NCO-2'). The inset of (d) is SEM images of NW arrays grown on Ti foils (NCO-2). Polarization curves were IR-compensated. Reproduced with permission.[11] Copyright 2014, Wiley-VCH. e) Chronopotentiometric curves for the OER on $Ni_xCo_{3-x}O_4$–1:1 electrode in 1.0 mol dm^{-3} NaOH at different current densities. Reproduced with permission.[55] Copyright 2011, Elsevier. f) ORR polarization curves of $NiCo_2O_4$–G, Co_3O_4–G, and 20 wt% Pt/C at a rotation rate of 900 rpm. OER CV curves of $NiCo_2O_4$–G, Co_3O_4–G, and 20 wt% Pt/C g) initial cycle and h) after 1000 CV cycles. Reproduced with permission.[105] Copyright 2013, Royal Society of Chemistry.

sion, such as in fuel cells and metal–air batteries.[122,123] Considerable research efforts have been made in developing an efficient and inexpensive catalyst for this field, and plenty of progress has been made exploring $NiCo_2O_4$-related electrocatalysts for ORR,[17,47,50,124] OER,[106,125–128] and bifunctional electrocatalysts for both reactions.[129,130] Starting from the $NiCo_2O_4$-related electrocatlysts for ORR, urchin-like $NiCo_2O_4$ spheres,[50] 3D macroporous $NiCo_2O_4$ sheets,[47] and hierarchical flower-like porous $NiCo_2O_4$ nanosheets[17] have been reported to exhibit high electrocatalytic activity and excellent long-term stability. Wang, Tang, and co-workers found that the air electrode based on $NiCo_2O_4$/CNT hybrids exhibited a superior catalytic performance even than the commercial Pt/C catalyst.[124] $NiCo_2O_4$ nanoparticles are smaller than 10 nm and homogeneously dispersed on the surface of carbon nanotubes (CNTs). The $NiCo_2O_4$/CNT electrode exhibits the highest current density, exceeding that of the Pt/C electrode, in the steady-state linear polarization test (**Figure 8**a), while similar results are observed in the galvanostatic discharge investigation at different discharge current densities. The enhancement of the $NiCo_2O_4$/CNT electrode is attributed to the synergistic effect between metal oxides and CNTs. CNTs not only serve as a dispersing support to prevent the catalyst's agglomeration but also to increase the whole electrical conductivity of the $NiCo_2O_4$/CNT hybrid and provide an effective conductive network for fast charge transfer during ORR. Can and co-workers prepared macroporous $NiCo_2O_4$ nanosheets with better long-term stability and stronger tolerance against methanol than Pt/C catalysts during ORR.[47] The macroporous $NiCo_2O_4$ nanosheets have a thickness of about 150 nm and pore volumes of 0.23 cm^3 g^{-1}. As shown in Figure 8b, the ORR current response retains almost the same with or without 2 M CH_3OH, indicating a high catalytic selectivity and remarkable methanol tolerance. During the long-term stability investigation by chronoamperometric measurements (Figure 8c), the steady current of $NiCo_2O_4$ nanosheet electrodes is significantly higher than that of Pt/C. Compared with the nearly 42% activity loss of the Pt/C electrode at 25 000 s, there is only about 30% activity loss for $NiCo_2O_4$ nanosheet electrodes up to 100 h. These features of $NiCo_2O_4$ nanosheet electrodes are very desirable for the development of alkaline fuel cells.

Nickel cobaltite also has gained considerable attention as an efficent and low-potential electrode for the oxygen evolution reaction in recent years as well.[11] Both morphological $NiCo_2O_4$ nanostructures such as nanowire arrays,[11,55] core-ring nanoplatelets,[38] hexagonal nanosheets,[126] nanorods[25] and various $NiCo_2O_4$ nanocomposites with aerogels,[125] graphene,[127] and Fe[128] are found to be favorable catalysts for the OER. Wu and co-workers fabricated $Ni_xCo_{3-x}O_4$ nanowire arrays (NW) on Ti foils and Ni foams respectively, and found that the $Ni_xCo_{3-x}O_4$ electrode with the 1:1 ratio of starting Ni:Co precursors exhibited a high electrocatalytic performance for ORR. Polarization curves (Figure 8d) of the $Ni_xCo_{3-x}O_4$ NW electrode at 1:1 ratio shows its superior catalytic performance.[11] The catalytic current density of this $Ni_xCo_{3-x}O_4$ NW electrode is up to six times higher than that of pure Co_3O_4 at the same potential. The chronopotentiometric investigation of the $Ni_xCo_{3-x}O_4$ NW electrode at a 1:1 ratio for OER (Figure 8e) exhibits nearly constant potentials at different current densities within the whole 10 h, indicating the excellent long-term stability of such nickel cobaltite electrodes.[55] Core-ring structured $NiCo_2O_4$

small NANO MICRO

nanoplates,[38] $NiCo_2O_4$ aerogels,[125] $NiCo_2O_4$ nanorods,[25] and porous nanosheet-stacked $NiCo_2O_4$ structures[126] are also found to be remarkable electrocatalysts for the OER with quite low overpotentials at 0.315 V (vs. SCE electrode), 0.184 V (vs. Hg/HgO electrode), ≈0.31 V (vs. Ag/AgCl electrode), and 0.438 V (vs. SCE electrode), respectively. Moreover, the nanocomposite of $NiCo_2O_4$ with other elements or substances can effectively improve its catalytic performance towards the OER. Bouzek and co-workers substituted Ni with Fe to fabricate a $Fe_xNi_{1-x}Co_2O_4$ nanocomposite and found a superior catalytic acivity at x = 0.1.[128] The water electrolysis test at a cell voltage of 1.85 V showed that the $Fe_{0.1}Ni_{0.9}Co_2O_4$ catalysts display a higher current density of 115 mA cm^{-2} than the 84 mA cm^{-2} of $NiCo_2O_4$, implying an improvement by doping with Fe. Qiao and co-workers prepared a 3D hybrid paper of N-doped porous graphene film–$NiCo_2O_4$ (PNG–NiCo) as an excellent OER catalyst.[106] At overpotentials of 373 mV and 564 mV, the catalytic current densities of PNG–NiCo electrodes are 5 mA cm^{-2} and 21.1 mA cm^{-2} respectively, which are comparable with that of noble metal catalysts. The enhancement of PNG–NiCo is ascribed to the advanced structural properties and dual-active-site mechanism. The hierarchically in-and-out-of-plane pores can provide high surface areas and facilitate mass transport for favorable kinetics. The hydrophilic functional groups of graphene make it easier to approach the electrolyte and anchor $NiCo_2O_4$. The 3D conductive networks can fully accommodate $NiCo_2O_4$ due to its unique layer-by-layer structure for a higher electrochemical stability. The dual-active-site mechanism provides two kinds of catalytic active sites, that is, $NiCo_2O_4$ iteself and strong N (O)–metal (Ni, Co) bonds from the interaction between $NiCo_2O_4$ and N-doped graphene,[131] which means more active sites are involved during OER. Lee and co-workers reported a self-assembled $NiCo_2O_4$–reduced graphene oxide nanocomposite ($NiCo_2O_4$-RGO), which exhibited a lower oxidation potential (0.135 V) and higher current density (4.1 mA cm^{-2}) than that of bare $NiCo_2O_4$ nanoparticles (0.33 V and 3.11 mA cm^{-2}).[127] These studies will promote further investigation into a wide range of $NiCo_2O_4$-related composites.

Developing bifunctional catalysts for both the oxygen reduction reaction and the oxygen evolution reaction have attracted increasing attention recently for the importance of two reactions in rechargeable metal–air batteries and water electrolyzers.[132] Since the remarkable performance of $NiCo_2O_4$ nanostructures towards ORR and OER, the exploration of $NiCo_2O_4$ nanostructures as bifunctional catalysts is significant.[56,73,105,129] Chen and co-workers reported that a hybrid material of mesoporous $NiCo_2O_4$ nanoplatelets and graphene sheets ($NiCo_2O_4$–G) served as an excellent bifunctional catalyst for both ORR and OER.[105] The $NiCo_2O_4$–G exhibits well-dispersed mesopores within the nanoplates with a large specific surface area of 77 m^2 g^{-1} and an average pore diameter of 11.8 nm. The ORR polarization investigation (Figure 8f) demonstrates the considerable improvement of $NiCO_2O_4$–G's onset potential and stable current density compared to that of Co_2O_4–G, although it is still not comparable with that of commercial Pt/C. But in the OER investigation by cyclic voltammetry (Figure 8g), the $NiCo_2O_4$–G exhibited a much lower onset potential and dramatically higher current density up to about 2 and 6 times more than that of Co_3O_4–G and Pt/C, respectively. Furthermore, after repeating the tests 1000 times (Figure 8h), the current density retention was up to 99.6% for the $NiCo_2O_4$–G hybrid, indicating a remarkably higher long-term stability than Pt/C. Shanmugam and co-workers reported 1D hierarchical $NiCo_2O_4$ nanostructures as efficient bifunctional catalysts for ORR and OER, which exhibit a much lower oxygen electrode activity of 0.84 V than those of commerical catalysts [Pt/C (1.16 V), Ru/C (1.01 V) and Ir/C (0.92 V)], indicating this kind of $NiCo_2O_4$ catalyst is a promising candidate for cathode materials of metal–air batteries.[73] $NiCo_2O_4$ bifunctional electrocatalysts can also be easily fabricated into gas diffusion electrodes (GDEs) without carbon components.[129,130] The bifunctional GDE not only avoids carbon corrosion at high potentials but also supports current densities up to 100 mA cm^{-2} with acceptable potentials.

The typical application of $NiCo_2O_4$ nanostructures as efficient bifunctional catalysts for ORR and OER is when serving as cathode catalysts for rechargeable Li–O_2 batteries.[31,54,133,134] Recently, Li–O_2 batteries have been regarded one of the most promising battery system candidates for future electrical vehicles.[135] It is well known that Li–O_2 batteries possesses a theoretical specific energy density of 3505 W h kg^{-1}, which is up to about ten times higher than the 387 W h kg^{-1} of Li-ion batteries,[136] but there are still several issues that hinder the current Li–O_2 batteries from practical applications, such as low energy efficiency, short cycle life, and low rate capability. The sluggish kinetics of the ORR and OER at the cathode will result in increasing polarization, raising the charge and discharge overpotentials. Therefore, the exploition of $NiCo_2O_4$ nanostructures as cathode materials for Li–O_2 with a higher reversible capacity, low charge/discharge overpotential, and long cycling stability is necessary. Cui and co-workers investigated mesoporous $NiCo_2O_4$ nanoflakes as efficient cathode catalysts for Li–O_2 batteries. The $NiCo_2O_4$-based electrode exhibits an effective electrocatalytic activity in nonaqueous phases with a larger current density in anodic scans and higher onset potential for the ORR than the super p-based (carbon) electrode. In the discharge/charge test, the $NiCo_2O_4$-based Li–O_2 electrode not only exhibits a lower overpotential than carbon-base electrodes, but also a much higher specifc capacity than those of carbon-based and Pt/C-based electrodes with stability over 10 cycles. Hierarchical macroporous/mesoporous $NiCo_2O_4$ nanosheets, ordered mesoporous $NiCo_2O_4$ materials, and hierarchical $NiCo_2O_4$ nanorods are found to be better candidates for Li–O_2 batteries than carbon black, with higher reversible capacities, lower overpotentials, and superior cycling stabilities.[45,133,134] Fu and co-workers assembled a novel Li–air battery with a hierarchical $NiCo_2O_4$ nanowire array/carbon cloth for clear observation of morphological changes of Li_2O_2 during the discharge/charge processes.[54] They found that porous ball-like Li_2O_2 deposited on the tips of $NiCo_2O_4$ nanowires during discharge, which are proposed to be the most active catalytic sites.

3.2.4. Anode Electrodes for Li-Ion Batteries

In order to meet the increasing demand of worldwide energy, high-power energy resources with a low cost and environmental friendliness have attracted more and more attention. Among various energy-storage systems, Li-ion batteries and supercapacitors are considered the most promising devices.[137] Due to their good electronic conductivity, superior electrochemical activity, high theoretical rate capacitance/capacity, and sufficient abundance, $NiCo_2O_4$ nanostructures are widely used as promising electrode materials for supercapacitors and Li-ion batteries. The advanced progress of $NiCo_2O_4$ in the field of supercapacitors has been systematically reviewed in up-to-date literature.[138,139] Therefore, the following content is focused on the application of $NiCo_2O_4$ nanostructrues as anode materials in Li-ion batteries.

Li-ion batteries have attracted increasing attention in both scientific and industrial fields as the main energy-storage devices for portable electronics and electric vehicles. Binary transition metal oxides have been considered ideal potential anode materials due to their variable oxidation states, reversible capacity, better structural stability, and higher electrical conductivity than a single metal oxide.[140] Among various bimetallic oxides, $NiCo_2O_4$ has been considered a promising anode material with large reversible capacity, good cycling stability and high recharge rate.[30,141] With a high theoretical capacity of 890 mA h g^{-1},[13] the whole electrochemical process of lithium extraction reactions at $NiCo_2O_4$ anode can be described as follows:[30]

$$NiCo_2O_4 + 8Li^+ + 8e^- \rightarrow Ni + 2Co + 4Li_2O \quad (6)$$

$$Ni + Li_2O \leftrightarrow NiO + 2Li^+ + 2e^- \quad (7)$$

$$Co + Li_2O \leftrightarrow CoO + 2Li^+ + 2e^- \quad (8)$$

$$CoO + 1/3Li_2O \leftrightarrow 1/3Co_3O_4 + 2/3Li^+ + 2/3e^- \quad (9)$$

$NiCo_2O_4$ nanostructures should be ingeniously fabricated to obtain anode materials with large specific surface areas for electrode/electrolyte contact, good electrolyte diffusion for Li-ion flux, and reduced volume changes during the charge/discharge process, which play an important role in their electrochemcial performance.[30,142] Xiong and co-workers fabricated monodisperse $NiCo_2O_4$ mesoporous microspheres with a high discharge capacity of 1198 mA h g^{-1}.[30] The $NiCo_2O_4$ microspheres display a mesoporous structure with a high specific surface area of 40.58 m^2 g^{-1} and a small pore diameter of 14.5 nm, which provides a large electrode/electrolyte contact area and benefits Li^+ transport and volume expansion/contraction. Hollow $NiCo_2O_4$ nanocubes,[74] urchin-like $NiCo_2O_4$ structures,[49] and $NiCo_2O_4$ nanorod arrays[59] also have been found to be good candidates as anode materials for Li-ion batteries with an appreciably smaller reversible capacity than $NiCo_2O_4$ mesoporous microspheres. Other than pure $NiCo_2O_4$ nanostructures, the composites of $NiCo_2O_4$ and other inorganic or carbon materials also exhibit excellent performance as anode materials for Li-ion batteries with distinctive advantages. Lu, Xu, and co-workers decorated $NiCo_2O_4$ nanotubes with Au nanoparticles to obtain $NiCo_2O_4$@Au nanotubes.[141] In $NiCo_2O_4$@Au nanotube anodes, Au nanoparticles not only improve the intrinsic conductivity of the electrode but also increase the electrode cycling stability by alleviating volume changes and phase damage during cycling. Wang and co-workers fabricated Fe_2O_3@$NiCo_2O_4$ porous nanocages, and the synergistic effect of binary components facilitates its performance for Li-ion batteries.[143] The nanocomposites of $NiCo_2O_4$ nanosturctures and carbon materials, such as negatively charged graphene oxide sheets,[89] reduced graphene oxide sheets,[90] carbon black,[144] and 3D hierarchical porous carbon[142] are another favourable strategy to improve the cycling performace of $NiCo_2O_4$. The carbon materials serve as conductive networks and facilitate electron transfer, resulting in an increase of conductivity of the whole anode. The graphene sheets can buffer the volume variations during the cycling process and release the lithiation-induced stress to benefit lithium storage and cycling stability.[89,90] For example, Xu, Lu, and co-workers synthesised $NiCo_2O_4$/graphene hybrid nanosheet arrays with a best reversible capacity of 1267 mA h g^{-1}.[89] Zhao, Zhou, and co-workers uniformly embedded $NiCo_2O_4$ nanoparticles into a 3DHPC (3D hierarchical porous carbon) matrix to fabricate $NiCo_2O_4$/3DHPC composite, whose initial discharge capacity reaches up to 1533 mA h g^{-1}.[142]

4. Summary and Future Perspectives

With the increasing studies of $NiCo_2O_4$ nanostructures in the past few years, the progress has been remarkable. Its unique properties and novel applications, such as for photodetectors, catalysts, electrode materials, and chemical sensors, reveal that $NiCo_2O_4$ nanostructures are promising materials for numerous fields. A series of morphological $NiCo_2O_4$ nanostructures such as nanowires, nanorods, nanotubes, nanosheets, nanoflakes, and hierarchical structures have been comprehensively prepared by numerous techniques: liquid-phase co-precipitation, hydro- and solvothermal routes, microwave-assisted methods, electrodeposition methods, electrospinning methods, and self-assembly. The liquid-phase co-precipitation and hydrothermal/solvothermal techniques are the most conventional because of their low cost, easy handling, and large-scale fabrication possibilites. The preparation strategy, calcination temperature, pretreatment conditions, and growth substrate tend to influence the textural, structural, and intrinsic properties of $NiCo_2O_4$ nanostructures and affect their performance. Nanocomposites of $NiCo_2O_4$ and diverse carbonaceous substrates are highly remarkable. Graphene, carbon nanotubes, carbon black, and amorphous carbon can all be used as substrates for $NiCo_2O_4$ hybrids. This series of carbon materials has been documented in a dual role as a supporting substrate, buffering mechanical stress and improving electrical conductivity notably. Therefore, the advantages in preparations and properties of the $NiCo_2O_4$ nanostructures have allowed diverse novel applications in the field of photoelectronics, catalysis, energy conversion, and storage.

At the same time, there is still a broad space for the development of $NiCo_2O_4$-related materials, and challenges remain in the exploiting and understanding of $NiCo_2O_4$ nanostructures in all fields. Herein, considerable further investigation and development of $NiCo_2O_4$ nanostructures is proposed. First, there are numerous $NiCo_2O_4$ nanostructures reported with different morphologies and applications, but the correlation mechanism of morphology/plane and application performance is still uncertain. Further theoritical derivation is quite necessary for an intensive understanding of the relationship between morphology and performance. A recent example arises from theoritical calculations of Co_3O_4 crystal planes for CO oxidation, where the catalytic reactivity is structure-sensitive and the Co_3O_4 (110) surface exhibits a higher reactivity than the (111) surface.[107] However, the fast development of efficient synthetic approaches will enable crystal orientation and the morphology-controlled preparation of $NiCo_2O_4$ nanostructures. The mechanism of morphology-dependent performance will be available with the help of theoritical calculations by then.

Second, the distribution of Ni and Co elements in Ni–Co binary oxides should be taken into account to promote application performance. Along with the change of the ratio of Ni and Co elements, the crystal structures can be altered from a NiO-type to a Co_3O_4-type structure. Wu and co-workers reported $Ni_xCo_{3-x}O_4$ nanowire arrays serving as a high-performance oxygen evolution catalysts with elemental Ni enriched on the nanowire surface.[11] Special attention should be paid to adjust the distribution of Ni and Co for better behavior.

Third, $NiCo_2O_4$ arrays have shown great scientific potential and technical application in energy conversion and storage, and the related studies of $NiCo_2O_4$ arrays can be extended to the field of photoelectronics and solar energy harvesting. Considerable progress has been made on the growth of various $NiCo_2O_4$ nanostructure arrays on diverse substrates, such as Ti foil or Ni foam. Hence, more comprehensive applications of $NiCo_2O_4$ arrays are qualified and imperative.

Finally, doping and blending with special materials is considered a facile and efficient strategy to improve the properties and enhance performance. Doping $NiCo_2O_4$ with Au, Fe_2O_3, graphene, or carbon nanotubes have been documented to facilitate a favorable effect. Exploration to tune the conductivity, bandgap, electronic, and optical properties of $NiCo_2O_4$ through doping or blending with other organic and inorganic materials will become a significant trend.

As one of the most interesting semiconductor oxides, $NiCo_2O_4$ nanostructures still have enormous potential in fundamental materials science and technological applications. Accordingly, we hope that the primary preparation strategies, typical examples, and our personal views in this article will interest the readers, providing a comprehensive background and brilliant ideas for the fabrication and application of $NiCo_2O_4$ nanostructures. It can be expected that progressive efforts in the design and utilization of $NiCo_2O_4$ nanostructures will develop into a momentous research area.

Acknowledgements

The work was supported by the National Natural Science Foundation of China (Grant Nos. 51471051 and 51372040), Science and Technology Commission of Shanghai Municipality (13NM1400300), Shanghai Shu Guang Project (12SG01), Innovation Program of Shanghai Municipal Education Commission (14ZZ003), the Programs for Professor of Special Appointment (Eastern Scholar) at Shanghai Institutions of Higher Learning, China Postdoctoral Science Foundation (2014M560294). The work was partially supported by the Deanship of Scientific Research, King Abdulaziz University under grant No. (47-130-35-HiCi).

[1] Q. Wang, B. Liu, X. Wang, S. Ran, L. Wang, D. Chen, G. Shen, *J. Mater. Chem.* **2012**, *22*, 21647.
[2] M. Lenglet, R. Guillamet, J. Durr, D. Gryffroy, R. E. Vandenberghe, *Solid State Commun.* **1990**, *74*, 1035.
[3] P. D. Battle, A. K. Cheetham, J. B. Goodenough, *Mater. Res. Bull.* **1979**, *14*, 1013.
[4] W. J. King, A. C. C. Tseung, *Electrochim. Acta* **1974**, *19*, 493.
[5] M. N. Iliev, P. Silwal, B. Loukya, R. Datta, D. H. Kim, N. D. Todorov, N. Pachauri, A. Gupta, *J. Appl. Phys.* **2013**, *114*, 033514.
[6] J. F. Marco, J. R. Gancedo, M. Gracia, J. L. Gautier, E. I. Rıos, H. M. Palmer, C. Greavesc, F. J. Berry, *J. Mater. Chem.* **2001**, *11*, 3087.
[7] L. Peng, L. F. Hu, X. S. Fang, *Adv. Funct. Mater.* **2014**, *24*, 2591.
[8] S. C. Han, L. F. Hu, N. Gao, A. A. Al-Ghamdi, X. S. Fang, *Adv. Funct. Mater.* **2014**, *24*, 3725.
[9] X. J. Xu, L. F. Hu, N. Gao, S. X. Liu, S. Wageh, A. A. Al-Ghamdi, A. Alshahrie, X. S. Fang, *Adv. Funct. Mater.* **2015**, *25*, 445.
[10] S. Han, D. Q. Wu, S. Li, F. Zhang, X. L. Feng, *Small* **2013**, *9*, 1173.
[11] Y. Li, P. Hasin, Y. Wu, *Adv. Mater.* **2010**, *22*, 1926.
[12] C. F. Windisch, G. J. Exarhos, K. F. Ferris, M. H. Engelhard, D. C. Stewart, *Thin Solid Films* **2001**, *398*, 45.
[13] R. Alcantara, M. Jaraba, P. Lavela, J. L. Tirado, *Chem. Mater.* **2002**, *14*, 2847.
[14] M. R. Tarasevich, B. N. Efremov, in *Electrodes of Conductive Metallic Oxides Part A* (Ed: S. Trasatti), Elsevier, USA **1982**, p.1227.
[15] L. F. Hu, L. Wu, M. Liao, X. Hu, X. S. Fang, *Adv. Funct. Mater.* **2012**, *22*, 998.
[16] Y. Gou, X. Liang, B. Chen, *J. Alloy Compd.* **2013**, *574*, 181.
[17] Z. Q. Liu, K. Xiao, Q. Z. Xu, N. Li, Y. Z. Su, H. J. Wang, S. Chen, *RSC Adv.* **2013**, *3*, 4372.
[18] B. Cui, H. Lin, Y. Z. Li, J. B. Li, P. Sun, X. C. Zhao, C. J. Liu, *J. Phys. Chem. C* **2009**, *113*, 14083.
[19] M. U. A. Prathap, R. Srivastava, *Electrochim. Acta* **2013**, *108*, 145.
[20] D. Wang, Z. Zou, J. Ye, *Chem. Phys. Lett.* **2003**, *373*, 191.
[21] F. K. Lotgering, *Philips Res. Rep.* **1956**, *11*, 337.
[22] G. Blasse, *Philips Res. Rep.* **1963**, *18*, 383.
[23] S. Verma, A. Kumar, D. Pravarthana, A. Deshpande, S. B. Ogale, S. M. Yusuf, *J. Phys. Chem. C* **2014**, *118*, 16246.
[24] S. Verma, H. M. Joshi, T. Jagadale, A. Chawla, R. Chandra, S. Ogale, *J. Phys. Chem. C* **2008**, *112*, 15106.
[25] N. Garg, M. Basu, K. Upadhyaya, S. M. Shivaprasad, A. K. Ganguli, *RSC Adv.* **2013**, *3*, 24328.
[26] M. Cabo, E. Pellicer, E. Rossinyol, M. Estrader, A. Lopez-Ortega, J. Nogues, O. Castell, S. Surinacha, M. D. Baro, *J. Mater. Chem.* **2010**, *20*, 7021.

[27] O. Knop, K. I. G. Reid, Sutarno, Y. Nakagawa, *Can. J. Chem.* **1968**, *46*, 3463.
[28] L. F. Hu, L. Wu, M. Liao, X. S. Fang, *Adv. Mater.* **2011**, *23*, 1988.
[29] G. Q. Zhang, H. B. Wu, H. E. Hoster, M. B. Chan-Park, X. W. Lou, *Energ. Environ. Sci.* **2012**, *5*, 9453.
[30] J. Li, S. Xiong, Y. Liu, Z. Ju, Y. Qian, *ACS Appl. Mater. Interface* **2013**, *5*, 981.
[31] L. X. Zhang, S. L. Zhang, K. J. Zhang, G. J. Xu, X. He, S. M. Dong, Z. H. Liu, C. S. Huang, L. Guo, G. L. Cui, *Chem. Commun.* **2013**, *49*, 3540.
[32] L. Qian, L. Gu, L. Yang, H. Yuan, D. Xiao, *Nanoscale* **2013**, *5*, 7388.
[33] P. Silwal, L. Miao, I. Stern, X. Zhou, J. Hu, D. H. Kim, *Appl. Phys. Lett.* **2012**, *100*, 032102.
[34] Q. A. Pankhurst, J. Connolly, S. K. Jones, J. Dobson, *J. Phys. D: Appl. Phys.* **2003**, *36*, R167.
[35] S. N. Kale, A. D. Jadhav, S. Verma, S. J. Koppikar, R. Kaul-Ghanekar, S. D. Dhole, S. B. Ogale, *Nanomed.: Nanotechnol., Biol. Med.* **2012**, *8*, 452.
[36] C. F. Windisch, K. F. Ferris, G. J. Exarhos, *J. Vac. Sci. Technol, A* **2001**, *19*, 1647.
[37] R. Bogglo, A. Carugati, G. Lodi, S. Trasatti, *J. Appl. Electrochem.* **1985**, *15*, 335.
[38] B. Cui, H. Lin, J. B. Li, X. Li, J. Yang, J. Tao, *Adv. Funct. Mater.* **2008**, *18*, 1440.
[39] A. Trunov, *Electrochim. Acta* **2013**, *105*, 506.
[40] R. Ding, L. Qi, M. Jia, H. Wang, *Electrochim. Acta.* **2013**, *113*, 290.
[41] R. Ding, L. Qi, M. Jia, H. Wang, *Catal. Sci. Technol.* **2013**, *3*, 3207.
[42] Q. Li, D. Tang, J. Tang, B. Su, G. Chen, M. Wei, *Biosens. Bioelectron.* **2011**, *27*, 153.
[43] C. Yuan, J. Li, L. Hou, L. Yang, L. Shen, X. Zhang, *J. Mater. Chem.* **2012**, *22*, 16084.
[44] H. Jiang, J. Ma, C. Z. Li, *Chem. Commun.* **2012**, *48*, 4465.
[45] B. Sun, J. Zhang, P. Munroe, H.-J. Ahn, G. Wang, *Electrochem. Commun.* **2013**, *31*, 88.
[46] L. Li, S. Peng, Y. Cheah, P. Teh, J. Wang, G. Wee, Y. Ko, C. Wong, M. Srinivasan, *Chem-Eur. J.* **2013**, *19*, 5892.
[47] Y. Xiao, C. Hu, L. Qu, C. Hu, M. Cao, *Chem—Eur. J.* **2013**, *19*, 14271.
[48] L. Yu, H. Wu, T. Wu, C. Yuan, *RSC Adv.* **2013**, *3*, 23709.
[49] H. S. Jadhav, R. S. Kalubarme, C. N. Park, J. Kim, C. J. Park, *Nanoscale* **2014**, *6*, 10071.
[50] Z. Q. Liu, Q. Z. Xu, J. Y. Wang, N. Li, S. H. Guo, Y. Z. Su, H. J. Wang, J. H. Zhang, S. Chen, *Int. J. Hydrogen Energ.* **2013**, *38*, 6657.
[51] X. Y. Yu, X. Z. Yao, T. Luo, Y. Jia, J. H. Liu, X. J. Huang, *ACS Appl. Mater. Interface* **2014**, *6*, 3689.
[52] T. Wu, J. Li, L. Hou, C. Yuan, L. Yang, X. Zhang, *Electrochim. Acta.* **2012**, *81*, 172.
[53] J. Xiao, S. Yang, *RSC Adv.* **2011**, *1*, 588.
[54] W. M. Liu, T. T. Gao, Y. Yang, Q. Sun, Z. W. Fu, *Phys.Chem.Chem. Phys.* **2013**, *15*, 15806.
[55] B. Lu, D. Cao, P. Wang, G. Wang, Y. Gao, *Int. J. Hydrogen Energ.* **2011**, *36*, 72.
[56] C. Jin, F. Lu, X. Cao, Z. Yang, R. Yang, *J. Mater. Chem. A* **2013**, *1*, 12170.
[57] L. Shen, Q. Che, H. Li, X. Zhang, *Adv. Funct. Mater.* **2014**, *24*, 2630.
[58] Q. F. Wang, X. F. Wang, B. Liu, G. Yu, X. J. Hou, D. Chen, G. Z. Shen, *J. Mater. Chem. A* **2013**, *1*, 2468.
[59] J. Liu, C. P. Liu, Y. L. Wan, W. Liu, Z. S. Ma, S. M. Ji, J. B. Wang, Y. C. Zhou, P. Hodgson, Y. C. Li, *CrystEngComm* **2013**, *15*, 1578.
[60] G. Zhang, X. W. Lou, *Sci. Rep.* **2013**, *3*, 1.
[61] J. Du, G. Zhou, H. Zhang, C. Cheng, J. Ma, W. Wei, L. Chen, T. Wang, *ACS Appl. Mater. Interface* **2013**, *5*, 7405.
[62] C. Yuan, J. Li, L. Hou, X. Zhang, L. Shen, X. W. Lou, *Adv. Funct. Mater.* **2012**, *22*, 4592.
[63] X. Y. Liu, Y. Q. Zhang, X. H. Xia, S. J. Shi, Y. Lu, X. L. Wang, C. D. Gu, J. P. Tu, *J. Power Sources* **2013**, *239*, 157.
[64] H. B. Wu, H. Pang, X. W. Lou, *Energy Environ. Sci.* **2013**, *6*, 3619.
[65] L. Li, Y. Cheah, Y. Ko, P. Teh, G. Wee, C. Wong, S. Peng, M. Srinivasan, *J. Mater. Chem. A* **2013**, *1*, 10935.
[66] J. Xiao, S. Yang, *J. Mater. Chem.* **2012**, *22*, 12253.
[67] S. Trasatti, *Transition Metal Oxides: Versatile Materials for Electrocatalysis in the Electrochemistry of Novel Materials*, (Ed: J. Lipkowski, P. N. Ross), VCH, Weinheim **1994**, 1207.
[68] J. F. Marco, J. R. Gancedo, M. Gracia, J. L. Gautier, E. Rios, F. J. Berry, *J. Solid State Chem.* **2000**, *153*, 74.
[69] M. Cabo, E. Pellicer, E. Rossinyol, O. Castell, S. Surinacn, M. D. Baro, *Cryst. Growth Des.* **2009**, *9*, 4814.
[70] C. Yuan, J. Li, L. Hou, J. Lin, G. Pang, L. Zhang, L. Lian, X. Zhang, *RSC Adv.* **2013**, *3*, 18573.
[71] F. Deng, L. Yu, G. Cheng, T. Lin, M. Sun, F. Ye, Y. Li, *J. Power. Sources* **2014**, *251*, 202.
[72] D. Carriazo, J. Patino, M. C. Gutierrez, M. Luisa Ferrer, F. del Monte, *RSC Adv.* **2013**, *3*, 13690.
[73] M. Prabu, K. Ketpang, S. Shanmugam, *Nanoscale* **2014**, *6*, 3173.
[74] H. Guo, L. Liu, T. Li, W. Chen, J. Liu, Y. Guo, Y. Guo, *Nanoscale* **2014**, *6*, 5491.
[75] Q. Zhou, J. Xing, Y. Gao, X. Lv, Y. He, Z. Guo, Y. Li, *ACS Appl. Mater. Interface.* **2014**, *6*, 11394.
[76] S. H. Yu, H. Colfen, M. J. Antoniietti, *J. Phys. Chem. B* **2003**, *107*, 7396.
[77] S. Raz, S. Weiner, L. Addadi, *Adv. Mater.* **2000**, *12*, 38.
[78] F. F. Cao, Y. G. Guo, L. J. Wan, *Energy Environ. Sci.* **2011**, *4*, 1634.
[79] L. Q. Mai, F. Yang, Y. L. Zhao, X. Xu, L. Xu, Y. Z. Luo, *Nat. Commun.* **2011**, *2*, 238.
[80] G. Zhang, X. W. Lou, *Adv. Mater.* **2013**, *25*, 976.
[81] H. Wang, X. Wang, *ACS Appl. Mater. Interface.* **2013**, *5*, 6255.
[82] F. Deng, L. Yu, M. Sun, T. Lin, G. Cheng, B. Lan, F. Ye, *Electrochim. Acta* **2014**, *133*, 382.
[83] R. R. Salunkhe, K. Jang, H. Yu, S. Yu, T. Ganesh, S. H. Han, H. Ahn, *J. Alloy Compd.* **2011**, *509*, 6677.
[84] X. Liu, S. Shi, Q. Xiong, L. Li, Y. Zhang, H. Tang, C. Gu, X. Wang, J. Tu, *ACS Appl. Mater. Interface* **2013**, *5*, 8790.
[85] W. Zhou, D. Kong, X. Jia, C. Ding, C. Cheng, G. Wen, *J. Mater. Chem. A* **2014**, *2*, 6310.
[86] P. Zhu, Y. Wu, M. V. Reddy, A. S. Nair, B. V. R. Chowdari, S. Ramakrishna, *RSC Adv.* **2012**, *2*, 531.
[87] M. S. S. G. Binitha, A. A. Madhavan, P. Praveen, A. Balakrishnan, K. R. V. Subramanian, M. V. Reddy, S. V. Nair, A. Sreekumaran Nair, N. Sivakumar, *J. Mater. Chem. A* **2013**, *1*, 11698.
[88] X. Wang, X. Han, M. Lim, N. Singh, C. L. Gan, M. Jan, P. S. Lee, *J. Phys. Chem. C* **2012**, *116*, 12448.
[89] Y. Chen, J. Zhu, B. Qu, B. Lu, Z. Xu, *Nano Energy* **2014**, *3*, 88.
[90] Y. Chen, M. Zhuo, J. Deng, Z. Xu, Q. Li, T. Wang, *J. Mater. Chem. A* **2014**, *2*, 4449.
[91] P. F. Ndione, A. Garcia, N. E. Widjonarko, A. K. Sigdel, K. X. Steirer, D. C. Olson, P. A. Parilla, D. S. Ginley, N. R. Armstong, R. E. Richards, E. L. Ratcliff, J. J. Berry, *Adv. Energy Mater.* **2013**, *3*, 524.
[92] G. Konstantatos, E. H. Sargent, *Nat. Nanotechnol.* **2010**, *5*, 391.
[93] F. Xia, T. Mueller, Y. M. Lin, A. Valdes-Garcia, P. Avouris, *Nat. Nanotechnol.* **2009**, *4*, 839.
[94] L. Li, P. Wu, X. S. Fang, T. Y. Zhai, L. Dai, M. Y. Liao, Y. Koide, H. Q. Wang, Y. Bando, D. Golberg, *Adv. Mater.* **2010**, *22*, 3161.
[95] L. F. Hu, M. Chen, X. S. Fang, L. M. Wu, *Chem. Soc. Rev.* **2012**, *41*, 1350.
[96] S. Mathur, S. Barth, H. Shen, J. C. Pyun, U. Werner, *Small* **2005**, *1*, 713.
[97] J. Zhou, Y. D. Gu, Y. F. Hu, W. J. Mai, P. H. Yeh, G. Bao, A. K. Sood, D. L. Polla, Z. L. Wang, *Appl. Phys. Lett.* **2009**, *94*, 191103.
[98] Y. Muraoka, N. Takubo, Z. Hiroi, *J. Appl. Phys.* **2009**, *105*, 103702.

[99] C. Yan, N. Singh, P. S. Lee, *Appl. Phys. Lett.* **2010**, *96*, 053108.
[100] N. J. Tharayil, S. Sagar, R. Raveendran, A. V. Vaidyan, *Physica B* **2007**, *399*, 1.
[101] A. Kudo, Y. Miseki, *Chem. Soc. Rev.* **2009**, *38*, 253.
[102] T. Swathi, G. Buvaneswari, *Mater. Lett.* **2008**, *62*, 3900.
[103] N. S. Chaubal, M. R. Sawant, *J. Mol. Catal. A-Chem.* **2007**, *261*, 232.
[104] B. M. Abu-Zied, S. A. Soliman, S. E. Abdellah, *Chinese J. Catal.* **2014**, *35*, 1105.
[105] D. U. Lee, B. J. Kim, Z. W. Chen, *J. Mater. Chem. A* **2013**, *1*, 4754.
[106] S. Chen, S.-Z. Qiao, *ACS Nano* **2013**, *7*, 10190.
[107] X. Y. Pang, C. Liu, D. C. Li, C. Q. Lv, G. C. Wang, *ChemPhysChem* **2013**, *14*, 204.
[108] M. V. Twigg, *Appl. Catal. B* **2007**, *70*, 2.
[109] A. Rohrbach, J. Hafner, G. Kresse, *Phys. Rev. B.* **2004**, *69*, 075413.
[110] D. Chu, R. Jiang, *Solid State Ionics* **2002**, *148*, 591.
[111] Y. Lu, J. P. Tu, C. D. Gu, X. H. Xia, X. L. Wang, S. X. Mao, *J. Mater. Chem.* **2011**, *21*, 4843.
[112] T. N. Danks, R. C. T. Slade, J. R. Varcoe, *J. Mater. Chem.* **2002**, *12*, 3371.
[113] R. Ding, L. Qi, M. Jia, H. Wang, *J. Power Sources* **2014**, *251*, 287.
[114] M. U. A. Prathap, R. Srivastava, *Nano Energy* **2013**, *2*, 1046.
[115] L. Gu, L. Qian, Y. Lei, Y. Wang, J. Li, H. Yuan, D. Xiao, *J. Power Sources* **2014**, *261*, 317.
[116] M. U. A. Prathap, B. Satpati, R. Srivastava, *Electrochim. Acta* **2014**, *130*, 368.
[117] H. L. Wang, Q. M. Gao, L. Jiang, *Small* **2011**, *7*, 2454.
[118] C. Z. Yuan, X. G. Zhang, L. H. Su, B. Gao, L. F. Shen, *J. Mater. Chem.* **2009**, *19*, 5772.
[119] G. Hu, C. Tang, C. Li, H. Li, Y. Wang, H. Gong, *J. Electrochem. Soc.* **2011**, *158*, A695.
[120] N. Spinner, W. E. Mustain, *Electrochim. Acta* **2011**, *56*, 5656.
[121] H. Heli, H. Yadegari, *Electrochim. Acta* **2010**, *55*, 2139.
[122] M. Lefevre, E. Proietti, F. Jaouen, J. P. Dodelet, *Science* **2009**, *324*, 71.
[123] G. Wu, K. L. More, C. M. Johnston, P. Zelenay, *Science* **2011**, *332*, 443.
[124] H. Zhang, H. Qiao, H. Wang, N. Zhou, J. Chen, Y. Tang, J. Li, C. Huang, *Nanoscale* **2014**, *6*, 10235.
[125] H. C. Chien, W. Y. Cheng, Y. H. Wang, T. Y. Wei, S. Y. Lu, *J. Mater. Chem.* **2011**, *21*, 18180.
[126] J. Yang, J. Li, H. Lin, X. Yang, X. Tong, G. Guo, *J. Appl. Electrochem.* **2006**, *36*, 945.
[127] M. Srivastava, M. E. Uddin, J. Singh, N. H. Kim, J. H. Lee, *J. Alloy Compd.* **2014**, *590*, 266.
[128] D. Chanda, J. Hnat, M. Paidar, K. Bouzek, *Int. J. Hydrogen Energ.* **2014**, *39*, 5713.
[129] X. Li, D. Pletcher, A. E. Russell, F. C. Walsh, R. G. A. Wills, S. F. Gorman, S. W. T. Price, S. J. Thompson, *Electrochem. Commun.* **2013**, *34*, 228.
[130] S. W. T. Price, S. J. Thompson, X. H. Li, S. F. Gorman, D. Pletcher, A. E. Russell, F. C. Walsh, R. G. A. Wills, *J. Power Sources* **2014**, *259*, 43.
[131] Y. Liang, Y. Li, H. Wang, J. Zhou, J. Wang, T. Regier, H. Dai, *Nat. Mater.* **2011**, *10*, 780.
[132] J. S. Lee, G. S. Park, H. I. Lee, S. T. Kim, R. Cao, M. Liu, J. Cho, *Nano Lett.* **2011**, *11*, 5362.
[133] B. Sun, X. Huang, S. Chen, Y. Zhao, J. Zhang, P. Munroe, G. Wang, *J. Mater. Chem. A* **2014**, *2*, 12053.
[134] Y. Li, L. Zou, J. Li, K. Guo, X. Dong, X. Li, X. Xue, H. Zhang, H. Yang, *Electrochim. Acta* **2014**, *129*, 14.
[135] H. G. Jung, J. Hassoun, J. B. Park, Y. K. Sun, B. Scrosati, *Nat. Chem.* **2012**, *4*, 579.
[136] P. G. Bruce, S. A. Freunberger, L. J. Hardwick, J. M. Tarascon, *Nat. Mater.* **2012**, *11*, 19.
[137] D. Y. Chen, X. Mei, G. Ji, M. H. Lu, J. P. Xie, J. M. Lu, J. Y. Lee, *Angew. Chem. Int. Ed.* **2012**, *51*, 2409.
[138] L. D. Feng, Y. F. Zhu, H. Y. Ding, C. Y. Ni, *J. Power Sources* **2014**, *267*, 430.
[139] D. P. Dubal, P. Gomez-Romero, B. R. Sankapal, R. Holze, *Nano Energy* **2015**, *11*, 377.
[140] Y. J. Chen, B. H. Qu, L. Mei, D. N. Lei, L. B. Chen, Q. H. Li, T. H. Wang, *J. Mater. Chem.* **2012**, *22*, 25373.
[141] J. Zhu, Z. Xu, B. Lu, *Nano Energy* **2014**, *7*, 114.
[142] L. Wang, L. Zhuo, C. Zhang, F. Zhao, *ACS Appl. Mater. Interface* **2014**, *6*, 10813.
[143] G. Huang, L. Zhang, F. Zhang, L. Wang, *Nanoscale* **2014**, *6*, 5509.
[144] Y. NuLi, P. Zhang, Z. Guo, H. Liu, J. Yang, *Electrochem. Solid State Lett.* **2008**, *11*, A64.
[145] T. Y. Wei, C. H. Chen, H. C. Chien, S. Y. Lu, C. C. Hu, *Adv. Mater.* **2010**, *22*, 347.
[146] X. F. Lu, D. J. Wu, R. Z. Li, Q. Li, S. H. Ye, Y. X. Tong, G. R. Li, *J. Mater. Chem. A* **2014**, *2*, 4706.
[147] W. W. Liu, C. X. Lu, K. Liang, B. K. Tay, *J. Mater. Chem. A* **2014**, *2*, 5100.
[148] F. Cai, Y. Kang, H. Chen, M. Chen, Q. Li, *J. Mater. Chem. A* **2014**, *2*, 11509.
[149] H. Wang, C. M. B. Holt, Z. Li, X. Tan, B. S. Amirkhiz, Z. Xu, B. C. Olsen, T. Stephenson, D. Mitlin, *Nano Res.* **2012**, *5*, 605.
[150] X. Wang, W. S. Liu, X. Lu, P. S. Lee, *J. Mater. Chem.* **2012**, *22*, 23114.
[151] W. Yang, Z. Gao, J. Ma, X. Zhang, J. Wang, J. Liu, *J. Mater. Chem. A* **2014**, *2*, 1448.
[152] L. Yu, G. Zhang, C. Yuan, X. W. Lou, *Chem. Commun.* **2013**, *49*, 137.
[153] G. Zhang, T. Wang, X. Yu, H. Zhang, H. Duan, B. Lu, *Nano Energy* **2013**, *2*, 586.

Received: February 1, 2015
Revised: April 6, 2015
Published online: June 29, 2015

